Scientific Reports

https://doi.org/10.1038/s41598-026-44490-9

Article in Press

Calcium-enriched mesoporous silica/PLGA scaffolds enhance bone repair in a rabbit femoral condylar defect model

Received: 16 September 2025

Accepted: 11 March 2026

Published online: 17 March 2026

Cite this article as: Wu H., Wu J., Tang H. *et al.* Calcium-enriched mesoporous silica/PLGA scaffolds enhance bone repair in a rabbit femoral condylar defect model. *Sci Rep* (2026). https://doi.org/10.1038/s41598-026-44490-9

Honghan Wu, Junxi Wu, Hao Tang, Qian Zhong, Guangquan Zhao, Qianyu Xie, Weikang Xu & Qingde Wa

Calcium-Enriched Mesoporous Silica/PLGA Scaffolds Enhance Bone Repair in a Rabbit Femoral Condylar Defect Model

Honghan Wu[a,1], Junxi Wu[c,1], Hao Tang[a,1], Qian Zhong[a], Guangquan Zhao[a], Qianyu Xie[a], Weikang Xu[b,**], Qingde Wa[a,*]

a Departament of Orthopadic Surgery, The Second Affiliate Hospital of Zunyi Medical University, zunyi 563000, China.

b Institute of Biological and Medical Engineering,Guangdong Academy of Sciences, Guangzhou 510632, China.

c Zunyi Medical University, zunyi 563000, China.

*Corresponding authors at: Departament of Orthopadic Surgery, The Second Affiliated Hospital of Zunyi Medical University , zunyi 563000, China.

** Correspondence to: Weikang Xu, Institute of Biological and Medical Engineering, Guangdong Academy of Sciences, Guangzhou 510632, China.

E-mail addresses:759200816@qq.com(W. Xu), wqd887zsy@126.com (Q. Wa).

[1]These authors contributed equally to this work.

Abstract

Bone defects resulting from trauma, tumors, or infection continue to pose significant clinical challenges, particularly when the defect size exceeds the capacity for spontaneous healing. In this study, we fabricated two types of composite scaffolds—calcium carbonate/mesoporous silica/poly(lactic-co-glycolic acid) (CMP) and mesoporous silica/poly(lactic-co-glycolic acid) (MP)—using a single-emulsion solvent evaporation method. Both scaffolds exhibited interconnected porous structures and favorable morphology. In vitro assays demonstrated that CMP scaffolds more effectively promoted

the proliferation and osteogenic differentiation of mesenchymal stem cells (MSCs) compared to MP scaffolds. Furthermore, a rabbit femoral condylar defect model was established to assess the in vivo bone regeneration efficacy and biocompatibility. Micro-CT imaging, along with hematoxylin-eosin (HE), Masson's trichrome, and Movat's pentachrome staining, as well as serum biochemical analyses, consistently indicated that CMP scaffolds significantly enhanced new bone formation and defect repair relative to MP scaffolds. Both scaffold types showed excellent tissue compatibility and elicited no adverse systemic effects. These findings suggest that calcium-enriched mesoporous silica/PLGA scaffolds hold strong potential as clinical biomaterials for the treatment of bone defects.

Keywords: Bone defect repair; In vivo evaluation; Calcium-enriched mesoporous silica/PLGA; Rabbit femoral defect model; Histological and micro-CT analysis

Introduction

Bone defects commonly arise from trauma, infection, tumors, or degenerative diseases such as osteoporosis, often resulting in substantial disruption of bone structure and function[1]. Although bone tissue exhibits intrinsic regenerative capacity, defects exceeding a critical size cannot heal spontaneously and therefore require exogenous intervention to facilitate and accelerate bone regeneration[2]. An ideal bone graft should exhibit excellent biodegradability and biocompatibility, while simultaneously supporting both osteoinduction and osteoconduction[3]. Currently, clinical strategies for bone defect repair include autografts, allografts, and synthetic bone substitutes[4].Autologous bone

grafting is considered the "gold standard" due to its superior osteogenic capacity and immunological compatibility. However, it is limited by donor site morbidity, infection risk, and insufficient availability[5,6]. While allografts can alleviate donor shortages, they are associated with immune rejection and potential disease transmission[7,8]. Consequently, the development of synthetic bone substitutes with favorable biological performance and controlled degradation characteristics has become a central focus in bone tissue engineering.

Among synthetic alternatives, three-dimensional (3D) scaffolds play a pivotal role by providing a structural framework for cell adhesion, proliferation, and differentiation, while mimicking the native bone matrix microenvironment to guide tissue regeneration[9]. Poly(lactic-co-glycolic acid) (PLGA) has been widely utilized in drug delivery and tissue engineering applications due to its biodegradability and favorable biocompatibility[10]. However, PLGA alone suffers from several limitations, including poor osteoconductivity, limited hydrophilicity, and suboptimal mechanical strength[11,12]. Previous studies have shown that PLGA in a 50:50 monomer ratio can be formulated into core–shell microspheres, promoting osteoblast proliferation and differentiation, with up to 75% new bone mineralization and mechanical properties approaching those of native bone in a rat model[13]. Despite these advantages, PLGA's low elastic modulus (~2 GPa) remains significantly below that of cortical bone (7–20 GPa), and its degradation generates acidic byproducts that may lead to local acidosis, impaired cell adhesion, and sterile inflammation[14-17]. These drawbacks considerably limit PLGA's application as a bone scaffold material.

To address these challenges, researchers have explored the incorporation of inorganic reinforcements into PLGA to enhance its mechanical and biological performance[18]. Among these, hexagonal mesoporous silica (HMS) has emerged as a promising additive due to its tunable pore size, large specific surface area, and excellent drug-loading capabilities[19,20]. HMS not only acts as a drug delivery matrix but also facilitates nutrient exchange, enhances intercellular signaling, and promotes tissue repair[21,22]. Recent studies have successfully integrated HMS with polymers such as polycaprolactone (PCL) to improve scaffold stiffness and flexibility[23]. Furthermore, composites of HMS with hydroxyapatite (HA) or other polymers have demonstrated increased compressive strength, elastic modulus, and improved cellular compatibility[24,25]. However, mismatches between scaffold degradation rates and the dynamic timeline of bone regeneration remain a concern, potentially hindering optimal tissue healing.

To further optimize the biological performance of scaffolds, the incorporation of calcium-based materials has gained considerable attention. Calcium carbonate (CC), a principal inorganic component of natural shells and coral, possesses excellent biocompatibility, biodegradability, and intrinsic pH buffering capacity[26,27].Within composite systems, CC can neutralize the acidic degradation products of PLGA, thereby stabilizing the local microenvironment and preventing acidosis-induced inhibition of osteoblast activity[28]. Moreover, calcium ions serve as critical signaling molecules in bone formation, directly participating in osteoblast differentiation and mineralization, and thus providing additional benefits for bone regeneration[29].

Building on this rationale, we developed a novel composite scaffold system by integrating CC and hexagonal mesoporous silica

(HMS) into a PLGA matrix using a single-emulsion solvent evaporation technique followed by low-temperature hot-melt processing. This approach leverages the pH-buffering capability of CC and the porous structural characteristics of HMS to synergistically enhance scaffold biocompatibility and osteoinductive capacity. In vitro studies were conducted to assess the effects of the CC/HMS/PLGA scaffold on mesenchymal stem cell (MSC) proliferation and osteogenic differentiation, while in vivo performance was systematically evaluated using a rabbit femoral condylar defect model (Figure 1). The results demonstrated that the composite scaffold significantly promotes new bone formation and achieves favorable tissue integration, offering promising insights and experimental evidence to support the clinical translation of synthetic bone graft materials.

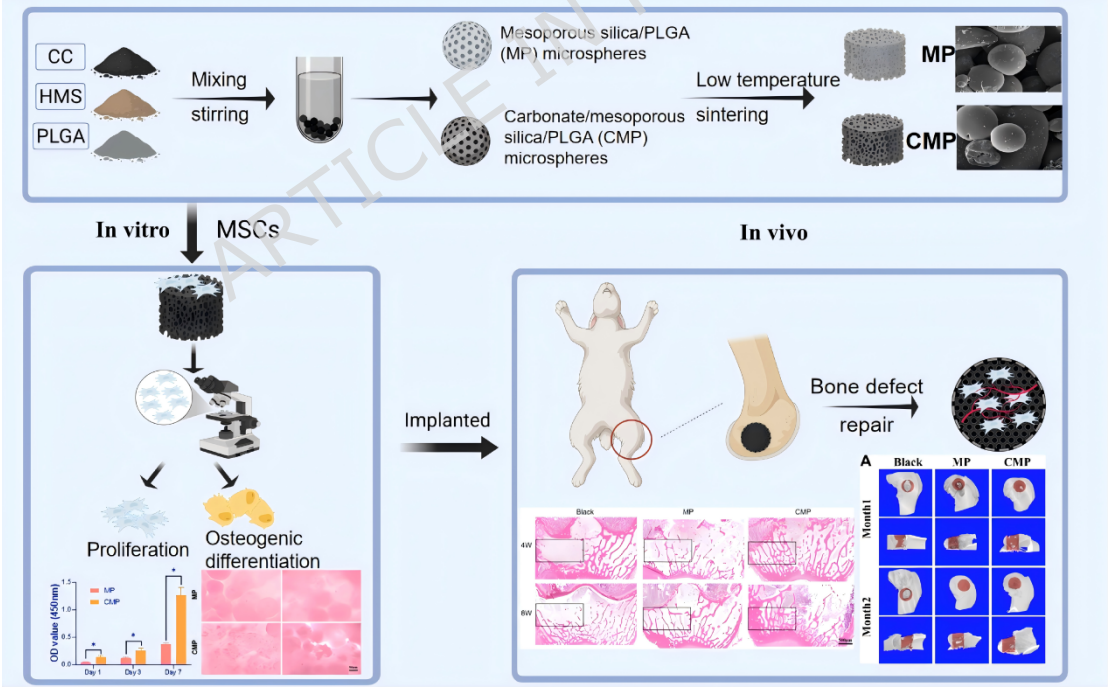

.Figure 1 Schematic illustration of the study design.

Materials and methods

Materials

Ethanol (EtOH) and dichloromethane were obtained from Guangzhou Chemical Reagent Factory (China). Dodecylamine, calcium carbonate (CC), and tetraethyl orthosilicate (TEOS) were purchased from Aladdin Chemical Co. (China). Poly(lactic-co-glycolic acid) (PLGA, 50:50 lactic acid:glycolic acid monomer ratio) was supplied by Daigang Biomaterials Co., Ltd. (Jinan, China). Mesenchymal stem cells (MSCs) were purchased from the American Type Culture Collection (ATCC, USA). Cell Counting Kit-8 (CCK-8) was purchased from Dojindo Laboratories (Japan), and osteogenic differentiation medium was obtained from Lonza (Switzerland).

Preparation of composite scaffold

(1)Synthesis of HMS

Five grams of dodecylamine were dissolved in a 70% (w/w) ethanol–water solution. TEOS was added dropwise under vigorous stirring at room temperature. The reaction mixture was allowed to stand undisturbed for 18 hours. The resulting precipitate was collected by filtration, dried at room temperature, and subjected to extraction at 80℃ for 24 hours to obtain purified HMS powder.

(2)Fabrication of HMS/PLGA and CC/HMS/PLGA Scaffolds

①HMS/PLGA scaffold: 1g of PLGA and 0.15 g of HMS particles were dispersed in 8 mL of dichloromethane and stirred for 2 minutes. Subsequently, 0.8% polyvinyl alcohol (PVA) aqueous solution was added, and the mixture was stirred for 10 hours. After solvent evaporation, the formed microspheres (MP) were collected, washed five times with deionized water, and dried. The dried MP microspheres were placed into a cylindrical mold and sintered at 70 ℃

for 2 hours to obtain the HMS/PLGA scaffold.

②CC/HMS/PLGA scaffold: 1g of PLGA, 0.15 g of HMS particles, and 0.1 g of CC were dispersed in 8 mL of dichloromethane and stirred for 2 minutes. The same emulsification and solvent evaporation procedure was followed using 0.8% PVA solution and 10-hour stirring. CMP microspheres were collected, washed five times with deionized water, and sintered at 70℃ for 2 hours in a cylindrical mold to form the final CC/HMS/PLGA scaffold.

Sterilization of composite Scaffolds

The dry MP microspheres and CMP microspheres were resp ectively placed into cylindrical models (with a diameter of 5 mill imeters and a height of 1 millimeter, as well as a diameter of 6 millimeters and a height of 10 millimeters), thereby obtaining t he MP scaffolds and CMP scaffolds for in vitro and in vivo studi es (Figure 2). Finally, the MP scaffolds and CMP scaffolds from the in vitro and in vivo studies were respectively sterilized with ^{60}Co-γ rays (15 kilograys).

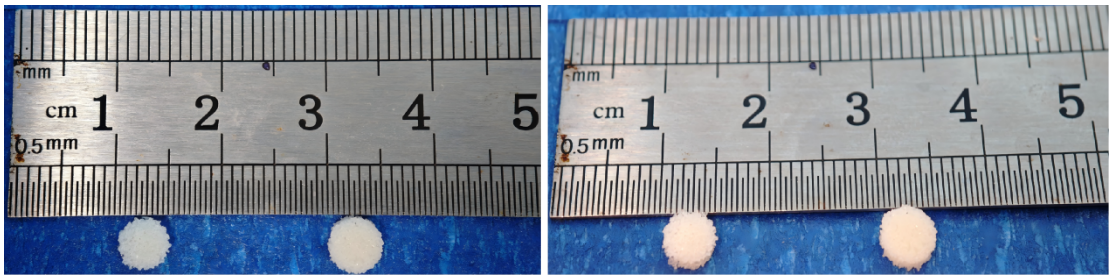

Figure 2 In vivo study of the scaffold(diameter 5mm, height 1mm).

Protein Adsorption Assay

Scaffolds (100 mg each of MP and CMP) were immersed in 150 μg/mL bovine serum albumin (BSA) in phosphate-buffered saline (PBS) and shaken at 25 rpm for 6 hours. After thorough washing with

PBS, the scaffolds were lysed in 1% sodium dodecyl sulfate (SDS), followed by centrifugation at 48 °C for 15 minutes. The protein content in the supernatant was quantified using the Bradford assay (Sigma-Aldrich, USA) and the MicroBCA™ Protein Assay Kit (Pierce, Rockford, IL, USA).

Measurement of Scaffold Density and Porosity

The dry mass of each scaffold was recorded as W. A known volume of anhydrous ethanol (V_1) was added to a graduated cylinder, and the scaffold was immersed in ethanol under vacuum cycles to ensure complete pore infiltration. After immersion, the ethanol volume was recorded as V_2. The scaffold was removed, and the remaining ethanol volume was recorded as V_3. The total scaffold volume was calculated as $V = V_2 - V_3$, and the pore volume as $V_p = V_1 - V_3$. Scaffold density and porosity were then calculated accordingly.

The surface morphology and elemental composition of the scaffold were observed using a scanning electron microscope and an EDS spectrometer.

Surface morphology of the MP and CMP scaffolds was examined using scanning electron microscopy (Nicolet™ iS20, Thermo, China). Prior to observation, samples were sputter-coated with gold using an SBC-12 mini ion coater. SEM imaging was performed at an accelerating voltage of 15 kV to characterize the surface microstructure of the composite microsphere scaffolds. Then, EDS was used to characterize the types of elements on the surface of each

group of scaffolds and the content of elements on the scaffold surface.

Recovery and Passage of MSCs Cells

When the mesenchymal stem cell (MSC) culture reaches 80–90% confluence, cells are considered ready for passaging. After the first passage, MSCs are continuously cultured in a CO_2 incubator until confluence is again achieved. Cells at passages 3 to 5 were selected for all subsequent in vitro experiments in this study to ensure stable growth characteristics.

CCK-8 cell proliferation assay

The proliferation of MSCs cultured on the scaffolds was assessed using the Cell Counting Kit-8 (CCK-8) assay. MSCs from passages 3 to 5 were seeded onto the surface of sterilized scaffolds and incubated under standard conditions. At predefined time points, CCK-8 reagent was added according to the manufacturer's protocol, and absorbance was measured to evaluate cell viability and proliferation.

Alkaline Phosphatase (ALP) Activity Assay

To assess osteogenic differentiation, ALP activity was measured on days 7 and 14 of culture. Scaffolds seeded with MSCs were pre-rinsed with PBS, and cells were gently detached. The cell lysates were prepared using 0.5 mL of PBS containing 0.1 M glycine, 1 mM $MgCl_2$, and 0.05% Triton X-100, incubated at 4 °C for 10 minutes. Lysates were sonicated twice for 30 seconds and then centrifuged at 12,300 rpm for 10 minutes at 4 °C. The supernatants were incubated with p-nitrophenyl phosphate (pNPP) substrate at 37 °C for 30 minutes. Total protein content was quantified using the MicroBCA

Protein Assay Kit, and ALP activity was normalized to total protein concentration.

Construction of animal model of femoral condyle bone defect

All experimental protocols of this study have been approved by the Medical Ethics Committee of Zunyi Medical University(ZMU21-2412-014), and all methods were carried out in accordance with relevant guidelines and regulations (the euthanasia method used in this study complies with the "AVMA Guidelines for the Euthanasia of Animals: 2020 Edition").Eighteen healthy New Zealand white rabbits (3 months old, ~4.0 kg) were randomly divided into three groups (n = 6 per group): (1) Blank group: bone defect created without scaffold implantation; (2) MP group: bone defect treated with HMS/PLGA (MP) scaffold; (3) CMP group: bone defect treated with CC/HMS/PLGA (CMP) scaffold.

A cylindrical bone defect (6 mm diameter × 10 mm depth) was created in the left femoral condyle under anesthesia. Scaffolds were sterilized using ultraviolet (UV) irradiation prior to implantation. In the blank group, only the defect was created; in the MP and CMP groups, the corresponding scaffold was implanted into the defect site. After implantation, the area was rinsed with sterile saline, disinfected with iodophor, and sutured. Postoperatively, rabbits were returned to standard housing conditions and administered intramuscular penicillin (800,000 U/day) for 3 consecutive days to prevent infection.

Specimen collection

(1)Blood sampling and specimen collection

At 4 and 8 weeks post-operation, 3 rabbits were randomly selected from each group for sample collection. Blood samples were

collected for biochemical analysis. Under anesthesia, the original incision was reopened to expose the femoral condyle defect area. Femoral condyles were obtained using a wire saw. After the bone tissue specimens were collected, the New Zealand rabbits were euthanized by ear vein injection . At the same time, liver and kidney tissues were collected for systemic biocompatibility assessment. All collected tissues (femur, liver and kidney) were fixed in 4% paraformaldehyde for subsequent histological and pathological analysis.

(2)Decalcification, embedding and sectioning

At 4 and 8 weeks postoperatively, the harvested femoral condyles, liver, and kidney tissues were fixed in 4% paraformaldehyde. Following fixation, samples were decalcified (for bone tissue), embedded in paraffin, and sectioned at a thickness of 5 μm using a rotary microtome for subsequent histological analysis.

Micro-CT imaging processing

Femoral condyle samples were fixed in 70–75% ethanol for a minimum of 48 hours. The fixed specimens were wrapped in ethanol-moistened cotton, placed into centrifuge tubes, and scanned using micro-computed tomography (Micro-CT). Scanning parameters were set as follows: resolution of 12 μm, 211°rotation angle, 0.2°rotation increment, 46 kV voltage, 75 μA current, and 80 ms exposure time. After scanning, the images were reconstructed in 3D for morphological assessment and quantitative analysis of new bone formation.

Hematoxylin and Eosin (H&E) Staining

Dehydration was performed by immersing sections in a graded ethanol series (70%, 80%, 90%, 95%, and 100%), with each step lasting 3 hours. Samples were then cleared in xylene for 15 minutes

and infiltrated with paraffin at 37 ℃ for 3 hours. Following embedding, paraffin blocks were sectioned (5 μm), floated in a 40℃ water bath, and dried. Sections were deparaffinized in xylene and rehydrated through descending ethanol concentrations. After rinsing in distilled water, slides were stained with hematoxylin for 3–8 minutes, differentiated in 1% hydrochloric acid ethanol for 30 seconds, and blued with ammonia water. Eosin staining was performed for 3–5 minutes. The slides were dehydrated through graded ethanol, cleared in xylene for 30 minutes, and mounted using neutral resin. Under the microscope, nuclei appear dark blue, while cytoplasm and fibrous tissues appear red.

Masson's *Trichrome Staining*

Sections were sequentially immersed in xylene I and II (20 minutes each), followed by absolute ethanol I and II (10 minutes each), then dehydrated through 70%, 80%, 90%, and 95% ethanol. After washing with distilled water, staining was carried out using a commercial Masson's trichrome staining kit. Slides were stained with Weigert's iron hematoxylin for 5–10 minutes, differentiated briefly in 1% hydrochloric acid ethanol, rinsed, and blued under running tap water. Acid fuchsin solution was applied for 5–10 minutes, followed by treatment with phosphomolybdic acid for 3–5 minutes. Aniline blue solution was then applied for 5 minutes, and sections were treated with 1% acetic acid for 1 minute. Dehydration was completed through graded ethanol and xylene (5 minutes in xylene I and II). Slides were sealed with neutral resin. Under microscopic observation, muscle fibers stain red and collagen fibers appear blue or green.

Movat's *Pentachrome Staining*

Slides were deparaffinized by immersion in xylene I and II (10 minutes each), followed by rehydration in descending alcohol concentrations (100%, 95%, 80%, and 70%; 2 minutes each), and rinsing with distilled water. Sections were stained with Alcian blue for 15 minutes, rinsed with tap water, and differentiated in preheated alkaline ethanol for 5 seconds. After rinsing, slides were stained with Weigert's hematoxylin for 60 minutes in the dark, followed by rinsing. Staining continued with fuchsin-O acid fuchsin for 3 minutes, followed by phosphomolybdic acid for 1 minute and acetic acid for 3 minutes (without washing between steps). Finally, slides were stained with tartrazine for 2 minutes, dehydrated in graded alcohol, cleared in xylene, and mounted. Under the microscope, various tissue components were distinguishable: nuclei (black), muscle fibers (red), collagen (yellow), ground substance and mucin (blue), and fibrin (bright red).

Statistical analysis

All experiments were performed in at least five independent replicates. Data are presented as mean ± standard deviation (Mean ± SD). Statistical analyses were conducted using IBM SPSS Statistics software (version 29.0). One-way analysis of variance (ANOVA) and independent-samples t-tests were employed to evaluate differences between groups. A p-value of < 0.05 was considered statistically significant. Graphs were generated using GraphPad Prism software.

Results

Scanning electron microscope image of the composite scaffold

The surface microstructure of the MP and CMP scaffolds was characterized by scanning electron microscopy (SEM). As shown

in Figure 3A, both scaffolds exhibited a porous structure based on microspheres, and the pore networks were interconnected. Both the MP stent and the CMP stent present a spherical appearance, and there are local protrusions and fine particles on the surface of both groups of stents.The chemical element analysis results obtained by energy dispersive spectrometer (EDS) indicated that the MP scaffold contained C, Si, and O elements, while the CMP scaffold contained Ca, C, Si, and O elements. This result indicates that calcium carbonate has been successfully introduced(Table 1,Figures 3B-D) .

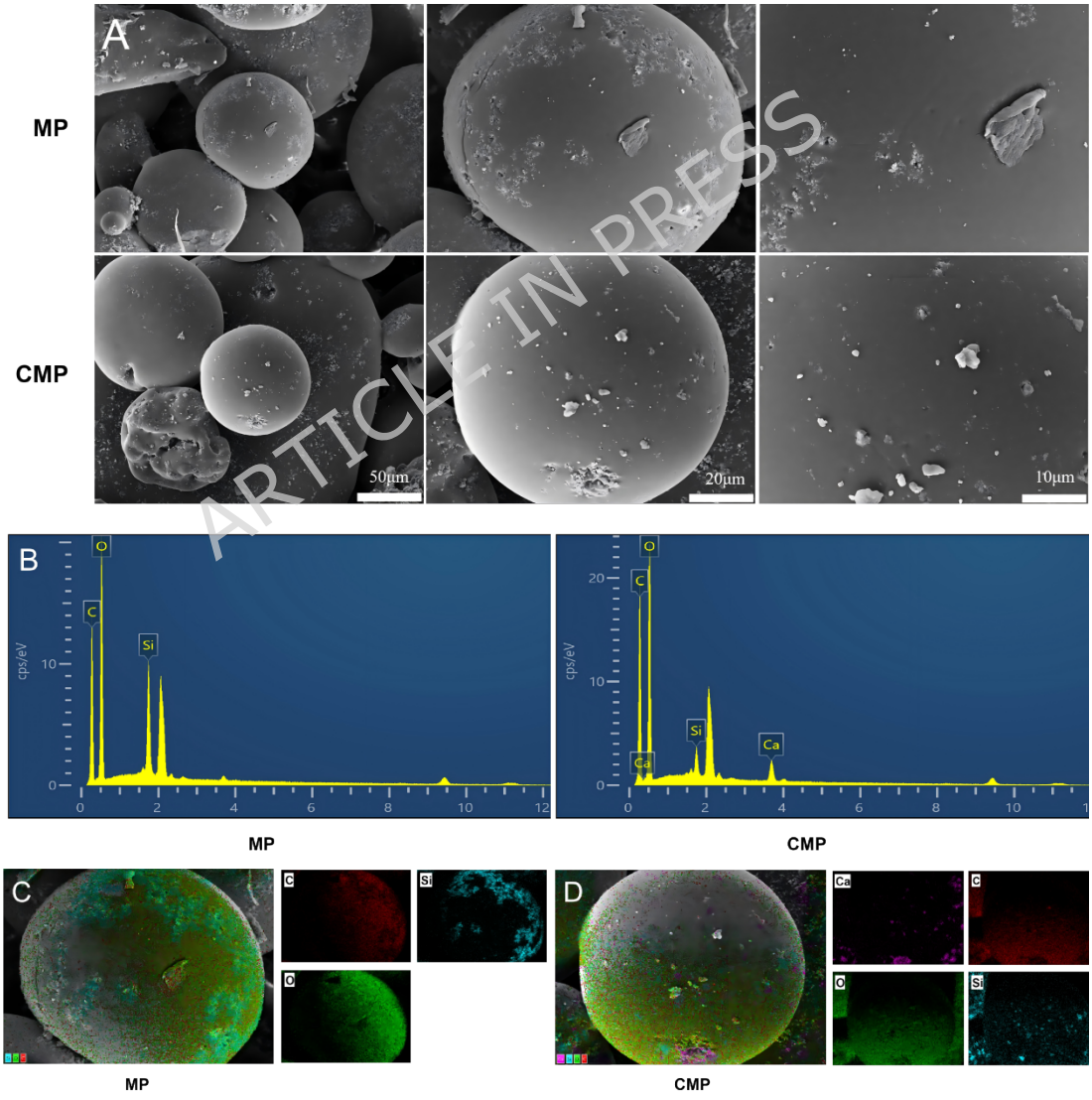

Table 1 Analysis of Element Composition of Stents in Each Group(Wt%)

Sample name	C（%）	Si（%）	O（%）	Ca（%）
MP	54.72	1.67	43.61	0
CMP	54.49	0.97	43.73	0.80

Figure 3. SEM images of MP and CMP scaffolds at different magnifications (Figure 3A), and EDS analysis of elements on the scaffold surface (Table 1, Figure 3 B-D).

The protein adsorption capacity of the composite scaffold

The protein adsorption capacity of the scaffolds was assessed by incubating samples in DMEM containing 1% bovine serum albumin (BSA). As shown in Figure 4C, the CMP scaffold exhibited significantly higher protein adsorption compared to the MP scaffold ($P < 0.01$), suggesting enhanced bioactivity and potential for improved cellular interaction.

Determination of the density and porosity of the composite scaffold

The density and porosity of the scaffolds were calculated using ethanol displacement, as described in the Methods section. Results demonstrated that the CMP scaffold had a significantly higher density than the MP scaffold ($P < 0.01$), as shown in Figure 4A. However, there was no statistically significant difference in porosity between the two groups ($P > 0.05$), as illustrated in Figure 4B.

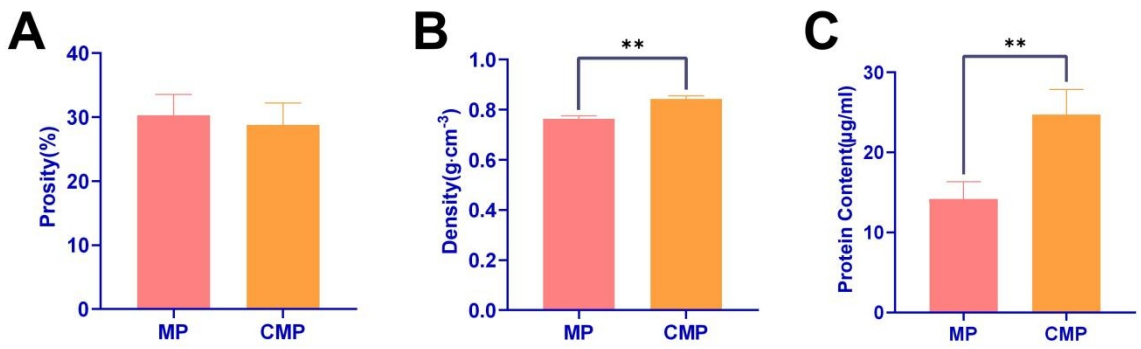

Figure 4. Quantitative analysis of (A) scaffold porosity, (B)scaffold density , and (C) protein adsorption capacity. Data are expressed as mean ± SD. ns: not significant ($P > 0.05$); **: $P < 0.01$.

The cell proliferation ability of the composite scaffold

The proliferation of MSCs seeded on MP and CMP scaffolds was evaluated at days 1, 3, and 7 using the CCK-8 assay. As shown in Figure 5 B, MSC proliferation on the CMP scaffold was significantly higher than on the MP scaffold at all time points ($P < 0.05$), indicating that the incorporation of calcium carbonate may enhance scaffold bioactivity and cell compatibility.

The Osteogenic Differentiation Capacity of Composite Scaffolds

To evaluate osteogenic potential, MSCs were cultured on MP and CMP scaffolds for 7 and 14 days. Alkaline phosphatase (ALP) staining revealed that the CMP group exhibited a higher staining intensity compared to the MP group at both time points (Figure 5 A1), indicating enhanced early osteogenic activity. Quantitative analysis of ALP activity (Figure 5 A2) showed a continuous increase over the culture period for both groups. Notably, ALP activity in the CMP group was significantly higher than that in the MP group on both day 7 and day 14 ($P < 0.05$), suggesting that the incorporation of calcium carbonate significantly promotes osteogenic differentiation of MSCs.

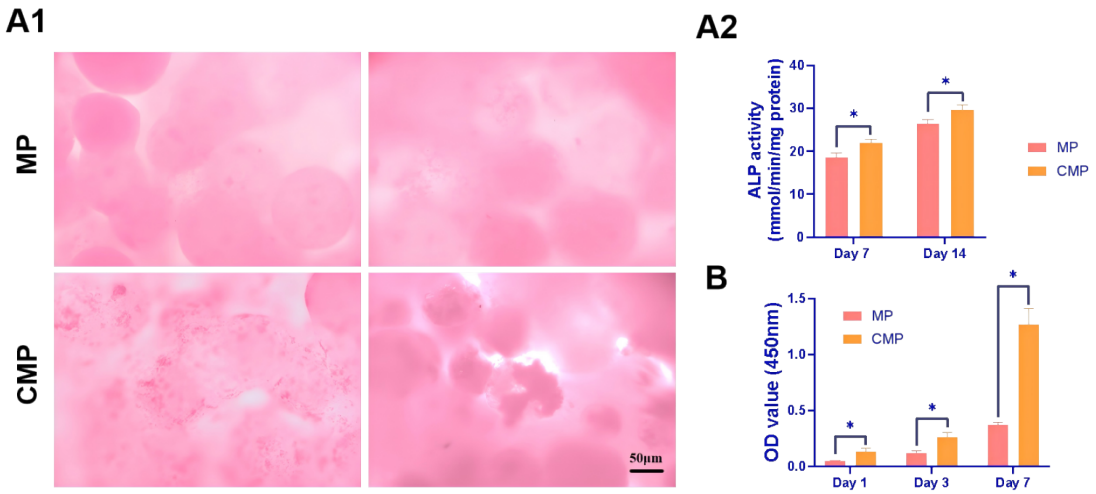

Figure 5. (A1) ALP staining of MSCs cultured on MP and CMP scaffolds on days 7 and 14. (A2) Quantitative analysis of ALP activity. (B) CCK-8 assay results showing MSC proliferation on MP and CMP scaffolds on days 1, 3, and 7. Data are presented as mean ± SD; *$P < 0.05$.

General observation of the rabbit femoral condyle defect model in New Zealand

All New Zealand white rabbits recovered well after surgery. On the day of the procedure, rabbits exhibited low activity levels and were withheld from food and water intake. By postoperative day 1, the rabbits ' mental status appeared normal, although activity remained limited. A small amount of food and water was reintroduced, and normal urination and defecation were observed. Surgical incisions were well-closed, with no signs of dehiscence. Daily intramuscular injections of penicillin were administered, and the incision area was disinfected.

On postoperative day 2, all rabbits resumed normal activity, with regular food and water intake, and no abnormalities in bowel or urinary function. Incisions remained clean and free of infection. The same postoperative care protocol was maintained.

By day 3, all rabbits returned to normal physiological behavior. No signs of incision-related complications were observed. One week post-surgery, wound healing was complete in all groups, and sutures were removed. No cases of bleeding, exudation, or localized swelling were reported, confirming the safety and tolerability of the implanted scaffolds.

Biocompatibility of the composite scaffold

(1)Blood Biochemical Analysis

Peripheral blood samples were collected from all experimental groups at weeks 4 and 8 postoperatively to assess systemic biocompatibility. As shown in Table 2, there were no statistically significant differences among the blank, MP, and CMP groups in white blood cell count (WBC), red blood cell count (RBC), hemoglobin (HB), platelet count (PLT), alanine aminotransferase (ALT), aspartate aminotransferase (AST), blood urea nitrogen (BUN), or creatinine (Cr) levels ($P > 0.05$). These results suggest that neither scaffold group induced hematological or organ function abnormalities.

Table 2. Hematological and liver/kidney function parameters in the blank, MP, and CMP groups at 4 and 8 weeks postoperatively.

	Test index	Black	MP	CMP	*P* value
4 W	WBC(10^9/L)	8.57±0.36	8.36±0.14	8.32±0.17	P=0.45
	RBC(10^{12}/L)	7.56±0.46	7.55±0.36	7.78±0.19	P=0.68
	HB(g/L)	135.33 ± 3.06	138.00±4.58	135.67±4.73	P=0.71

	PLT(10^9/L)	555.33 ± 29.54	565.33 ± 37.21	560.33±39.17	P=0.94
	ALT(U/L)	44.30±3.59	44.37±2.66	47.03±2.73	*P*=0.49
	AST(U/L)	58.13±2.82	58.93±4.24	57.93±3.27	*P*=0.93
	BUN(mmol/L)	14.77±1.96	14.87±1.26	15.10±0.82	*P*=0.96
	Cr(μmol/L)	116.33 ± 4.16	120.67±7.57	120.00±4.36	*P*=0.62
8 W	WBC(10^9/L)	8.54±0.17	8.43±0.59	8.49±0.11	*P*=0.93
	RBC(10^{12}/L)	7.62±0.36	7.43±0.44	7.74±0.28	*P*=0.61
	HB(g/L)	138.00 ± 6.08	136.33±4.73	137.00±3.61	*P*=0.92
	PLT(10^9/L)	565.00 ± 25.87	587.67 ± 12.74	588.33±13.65	*P*=0.29
	ALT(U/L)	47.00±2.89	46.83±3.68	44.20±1.55	*P*=0.45
	AST(U/L)	59.10±2.88	60.37±4.45	59.73±3.29	*P*=0.91
	BUN(mmol/L)	16.07±1.15	15.03±1.63	15.17±1.22	*P*=0.62
	Cr(μmol/L)	117.00 ± 3.00	122.67±5.51	117.67±13.32	*P*=0.69

(2) HE staining of liver and kidney tissues

To determine whether the two groups of composite scaffolds were toxic in New Zealand rabbits, liver and kidney samples were collected from the three groups of rabbits at the 4th and 8th weeks after surgery and prepared into sections. After HE staining, the samples were observed under a microscope. The HE staining of liver and kidney tissues revealed that in each group, liver cells, central veins, and hepatic sinusoids could be observed, and in each group, kidney glomeruli and renal tubules could also be seen. The morphology was normal. No obvious inflammatory cell infiltration was observed in the liver and kidney tissues of the three groups of New Zealand rabbits, indicating that the two groups of composite scaffolds had no significant toxicity (Figures 6 and 7).

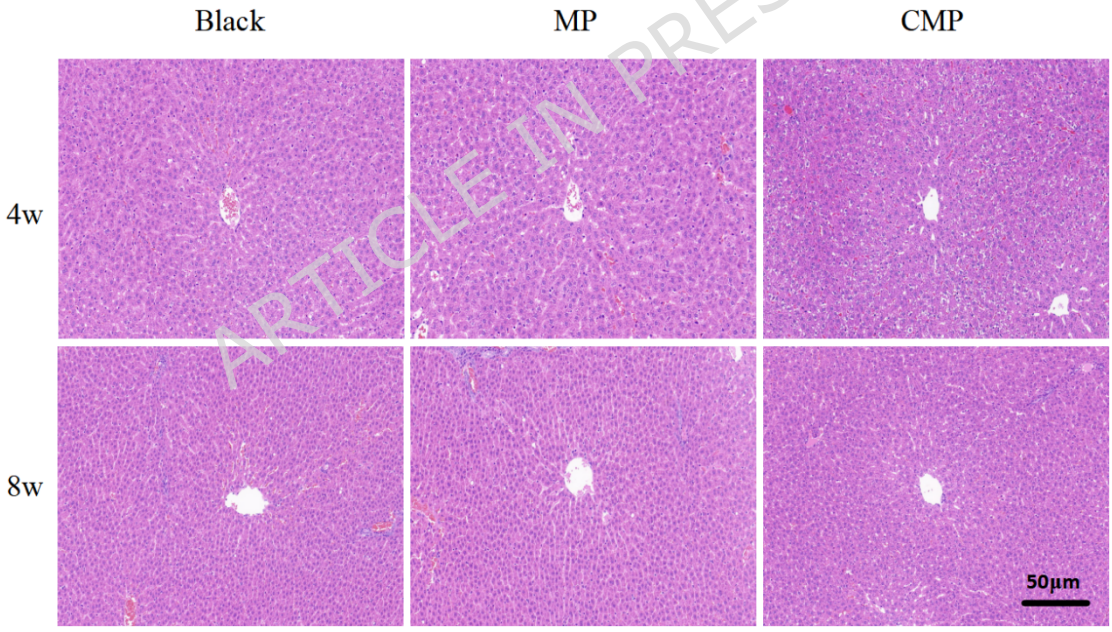

Figure 6. H&E staining of liver tissue at weeks 4 and 8 post-implantation in the blank, MP, and CMP groups (scale bar = 50 μm).

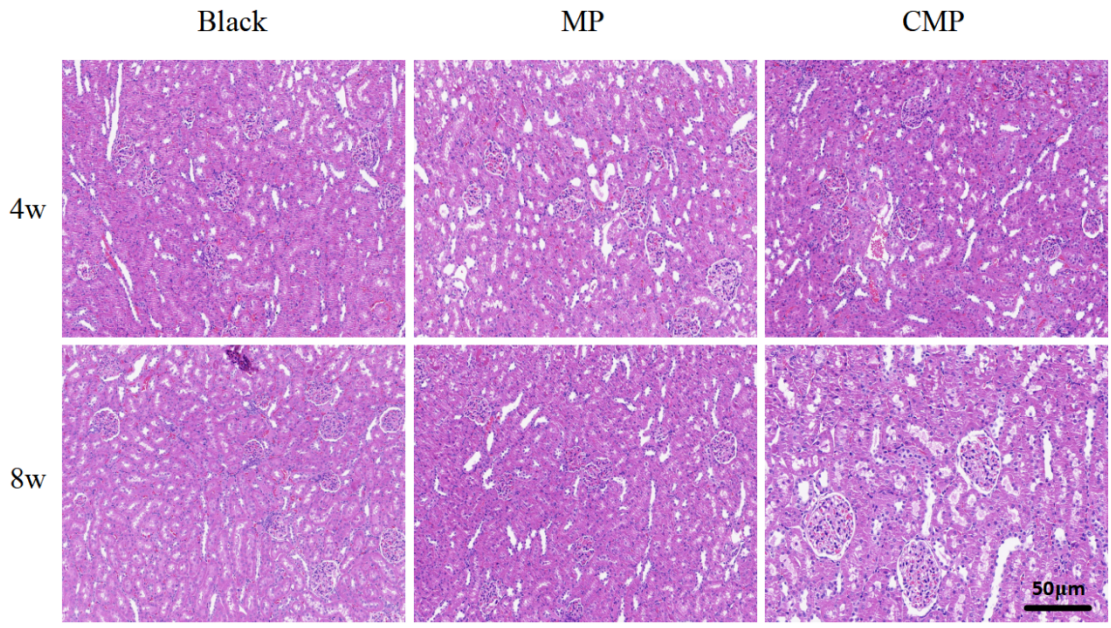

Figure 7. H&E staining of kidney tissue at weeks 4 and 8 post-implantation in the blank, MP, and CMP groups (scale bar = 50 μm).

The osteogenic ability of the composite scaffold

(1)Micro-CT examination

Micro-computed tomography (Micro-CT) was performed at 4 and 8 weeks postoperatively to assess new bone formation in the femoral condyle defect areas of the blank, MP, and CMP groups. At 4 weeks, all groups exhibited varying degrees of new bone formation. The CMP group demonstrated the most extensive new bone area, followed by the MP group, while only minimal new bone tissue was observed in the blank group. By 8 weeks, the CMP group showed further progression in bone regeneration, with a noticeably larger volume of new bone compared to both the MP and blank groups. The MP group exhibited a modest increase in bone formation, while the blank group continued to present with a large unhealed defect (Figure 8A).

Quantitative analysis of bone volume fraction (BV/TV) was conducted to evaluate the extent of bone regeneration. As shown in Figure 8B, the CMP group displayed significantly higher BV/TV values than both the MP and blank groups at both 4 and 8 weeks

post-surgery ($P < 0.05$), confirming the superior osteogenic performance of the calcium-enriched scaffold.

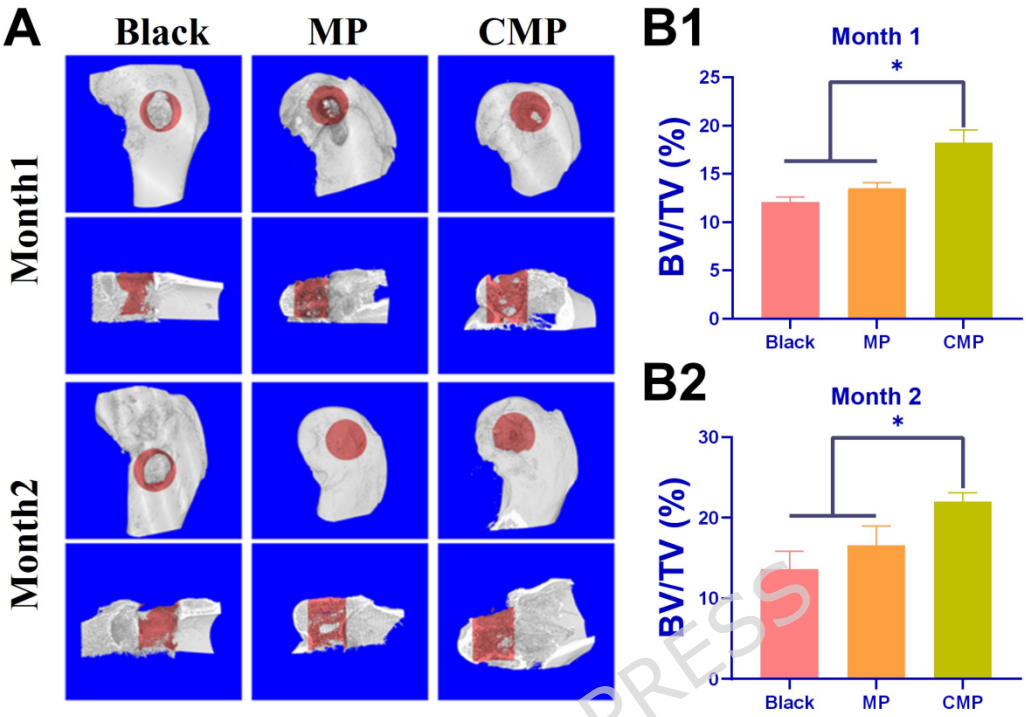

Figure 8. (A) Micro-CT images of the femoral condyle defect sites at 4 and 8 weeks post-surgery. (B) Quantification of bone volume fraction (BV/TV) in the blank, MP, and CMP groups. Data are presented as mean ± SD; *$P < 0.05$.

(2)Histological Evaluation of Bone Regeneration

To further verify the bone regenerative capacity of the composite scaffolds, hematoxylin and eosin (H&E) staining was performed on femoral condyle tissue sections collected at 4 and 8 weeks postoperatively. At 4 weeks, the CMP group displayed abundant new trabecular bone within the defect region, whereas the MP group showed fewer, sparsely distributed trabeculae. In contrast, the blank group exhibited little to no evidence of new bone formation. By 8 weeks, the CMP group exhibited increased trabecular density and maturation, with more extensive new bone tissue compared to the MP and blank groups. The MP group showed a slight increase in trabecular bone formation,

while the blank group continued to demonstrate limited osteogenesis (Figure 9).

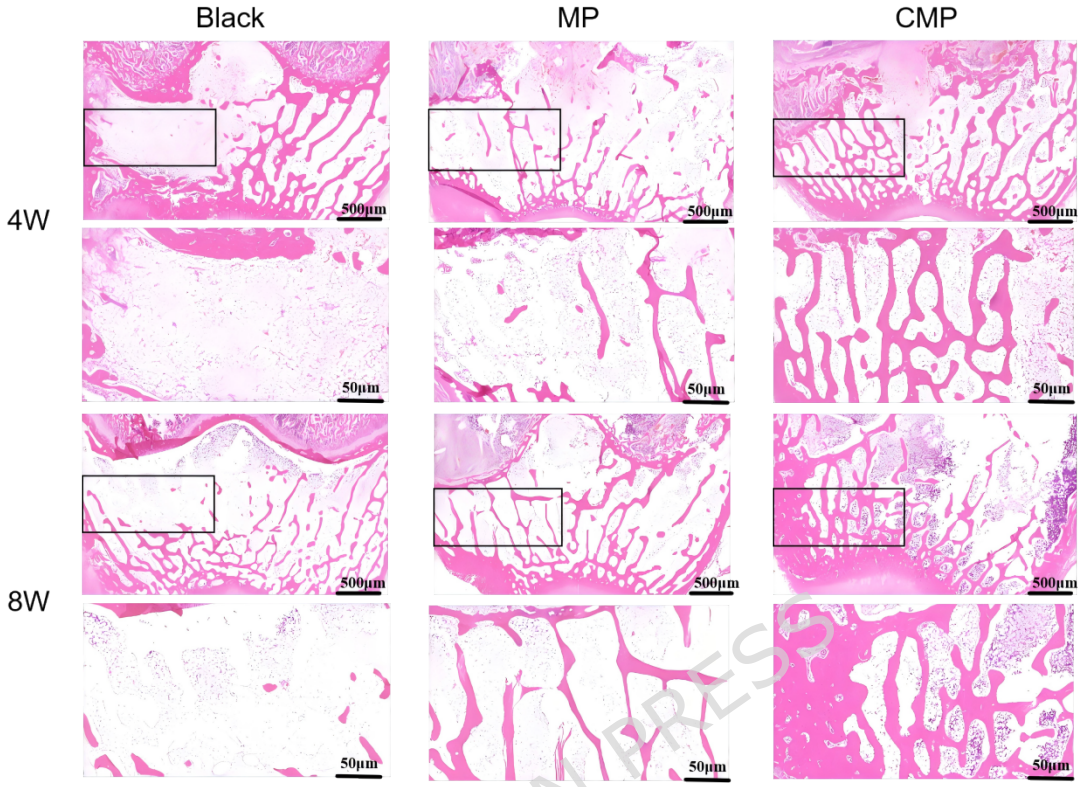

Figure 9. H&E staining of femoral condyle defect regions in the blank, MP, and CMP groups at 4 and 8 weeks post-surgery.

(3)Masson's Trichrome Staining of Femoral Condyle Tissue

Masson's trichrome staining was performed to evaluate collagen deposition and muscle fiber regeneration in the defect sites. At 4 weeks post-implantation, the CMP group exhibited abundant blue-stained collagen fibers and red-stained muscle fibers, indicating active extracellular matrix deposition and tissue remodeling. The MP group showed a moderate level of collagen and muscle fiber formation, while the blank group presented with minimal staining. By 8 weeks, the CMP group displayed a further increase in collagen and muscle fiber content, surpassing that of the MP and blank groups. The MP group showed a slight increase in matrix deposition compared to 4 weeks, while the blank group remained largely unchanged, with limited tissue

regeneration (Figure 10).

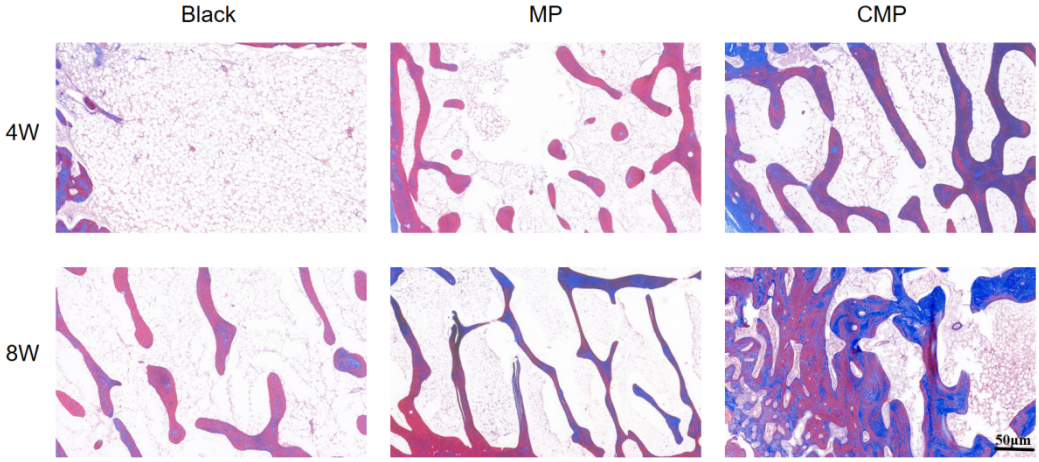

Figure 10. Masson's trichrome staining of bone defect regions in the blank, MP, and CMP groups at 4 and 8 weeks post-surgery (scale bar = 50 μm).

(4)Movat's Pentachrome Staining of Femoral Condyle Tissue

Movat's pentachrome staining was used to further assess the composition of the regenerating bone tissue. At 4 weeks, the CMP group showed extensive deposition of yellow-stained collagen fibers and reticular fibers, consistent with active matrix remodeling. In contrast, the MP group showed limited fiber formation, and the blank group exhibited negligible extracellular matrix staining.

At 8 weeks, the amount and distribution of collagen and reticular fibers increased substantially in the CMP group, indicating progressive tissue maturation. The MP group showed moderate improvement, while the blank group displayed only sparse fiber deposition (Figure 11).

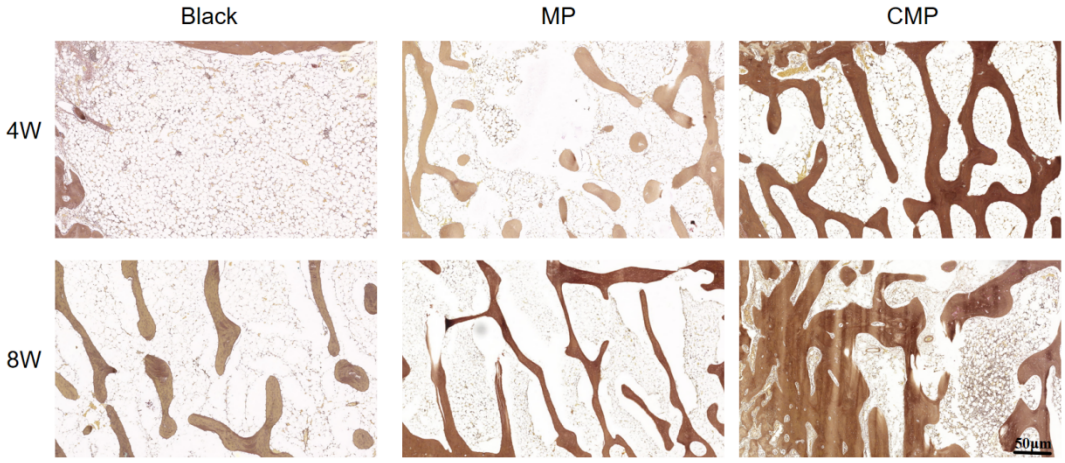

Figure 11. Movat's pentachrome staining of bone defect areas in the blank, MP, and CMP groups at 4 and 8 weeks post-surgery (scale bar = 50 μm).

Discussion

Through comprehensive in vitro and in vivo assessments, this study confirmed the superior performance of the calcium carbonate/hexagonal mesoporous silica/PLGA (CMP) composite scaffold over the mesoporous silica/PLGA (MP) scaffold in bone defect repair. The energy dispersive spectroscopy (EDS) analyzer analyzed the elemental composition of the scaffold surface and found that calcium elements could be detected on the surface of the CMP scaffold, indicating that the calcium carbonate was successfully introduced into the scaffold, thus confirming the successful preparation of the CMP scaffold(Table 1, **Figures 3B-D)**. The CMP scaffold demonstrated enhanced cell compatibility, protein adsorption capacity, osteogenic differentiation, and in vivo bone regeneration compared to the MP scaffold. The superior performance of the CMP scaffold in promoting mesenchymal stem cell (MSC) proliferation and osteogenic differentiation is likely attributed to its optimized surface physicochemical properties and improved pore architecture (**Figures 2, 4A, 4B**). Increased surface roughness and higher porosity render the scaffold more biomimetic,

resembling the microstructure of natural cancellous bone. This structural similarity facilitates better cell adhesion and spreading, essential for osteogenesis[30]. The previous experimental results showed that the CMP scaffold also significantly outperformed the pure PLGA scaffold in protein adsorption ability (**Figure 4C**), and it could accumulate more adhesive proteins (such as fibronectin) in a culture environment containing 10% FBS, providing more initial adhesion sites for MSCs[31-34]. Existing studies have shown that the Arg-Gly-Asp (RGD) sequence in fibronectin can mediate cell-matrix binding and is an important factor for promoting cell adhesion[35, 36].Moreover, the presence of $CaCO_3$ and HMS improved the hydrophilicity of the CMP scaffold, enhancing its ability to adsorb not only proteins but also essential nutrients. This, in turn, supported improved cell colonization and proliferation[37]. These results align with previous findings demonstrating that $CaCO_3$ incorporation into PLGA can significantly enhance cell adhesion and proliferation **(Figures 5B)**, further validating the cytocompatibility of CMP scaffolds [38, 39]. Beyond protein interaction, the scaffold's porosity and density also play a critical role in modulating cell behavior and facilitating bone regeneration. CMP scaffolds exhibited higher porosity and slightly lower density than MP scaffolds. These features increased the material's surface area, enabling more effective cell attachment and nutrient exchange, while also promoting cellular infiltration and neovascularization[40-42]. In natural bone, cortical bone exhibits porosity of approximately 5–10%, whereas cancellous bone reaches 30–95% porosity. Such highly porous architecture supports the metabolic activity and regenerative capacity of bone tissue[43, 44]. Replicating this multi-scale, porous microstructure enhances cellular migration and vascular penetration, both of which are critical for tissue remodeling and regeneration [45]. ALPis a

hallmark enzyme of early osteoblast differentiation and plays a crucial role in bone mineralization by increasing local phosphate concentration and degrading inhibitors of calcium deposition[46]. The results of this study show that at 7 days and 14 days of culture, the ALP staining density and activity of CMP scaffolds were significantly higher than those of the MP group **(**$P < 0.05$, **Figures 5 A1, A2**), suggesting that CMP can effectively promote osteogenic differentiation of MSCs in vitro. To accurately evaluate the osteogenic effect and biological safety of the scaffold in vivo, choosing an appropriate animal model is crucial. Rabbits, due to their complete bone structure and typical Havre system, and the ease of operation, are widely used in bone defect research[47, 48]. Among them, New Zealand white rabbits, because their bones are similar in size and repair speed to humans, are often chosen as the preferred animals for establishing bone defect models[49]. In this study, The femoral condyle defect model closely mimics clinical bone injury conditions, offering a reliable platform for evaluating scaffold integration and regenerative efficacy.

Micro-CT and histological analyses confirmed that the CMP scaffold promoted robust trabecular bone formation and supported vascular and tissue ingrowth (**Figures 8–11**). These outcomes can be attributed to the optimized surface topography and internal pore architecture of the CMP scaffold, which together create a favorable microenvironment that mimics native bone. This structural and biochemical optimization underpins the enhanced osteogenic outcomes observed in the CMP group compared to the MP scaffold.

The histological analysis results of this study were consistent with the Micro-CT results. HE, Masson, and Movat staining all showed that the CMP group had more bone trabeculae and collagen fibers generated at 4 and 8 weeks after surgery, and the repair of

the bone defect area was significantly better than that of the MP group (**Figures 9-11**). Notably, the CMP scaffold provided early mechanical support while maintaining a good degradation match with the new bone formation process. This metabolic coordination characteristic reduced the adverse effects of long-term residual materials on tissue repair[50, 51]. Compared with the PLGA/HMS-HA composite scaffold reported by previous studies[25], the CMP scaffold improved mechanical properties and promoted osteogenesis while introducing $CaCO_3$ to achieve more effective neutralization of acidic by-products, demonstrating more comprehensive performance advantages. In the fourth week, no obvious debris from the stent was observed, indicating that the macroscopic degradation rate of the stent was relatively fast. However, this does not mean that the stent no longer affects the healing process thereafter. We believe that the main function of the stent is manifested in the early stage (0-4 weeks), specifically as follows: promoting early vascularization, as well as enhancing osteogenic differentiation and extracellular matrix deposition[29]. These early events establish a favorable healing trajectory for osteogenesis. The excellent bone formation observed at the 8th week mainly reflects the cumulative and continuous downstream effects (matrix maturation and mineralization), rather than the physical presence of the stent in the later stage[52]. Moreover, even if no macroscopic debris is detected, micrometer/nanometer-level degradation products and/or ion exchange may be locally present and contribute to bone conductive mineralization[53].Additionally, CC can release Ca^{2+} and bind to calmodulin (CaM) to form a complex, which promotes osteoblast differentiation and matrix mineralization through corresponding signaling pathways[54]. The silicon ions released by HMS upregulated the expression of osteogenic genes and collagen

proteins[55]. This advantage is not only reflected in the proliferation and differentiation of cells, but also achieved stable and significant bone defect repair effects in animal models.

The in vivo biocompatibility of the scaffolds was further validated through comprehensive histopathological and blood biochemical analyses. H&E staining of liver and kidney tissues, along with peripheral blood indices, showed no significant pathological alterations across all experimental groups (**Table 2; Figures 6 and 7**), indicating low systemic toxicity and excellent tissue compatibility. These findings are consistent with previous studies reporting that PLGA possesses inherent biocompatibility and degradability, while $CaCO_3$ serves as a bioactive, non-toxic additive that enhances both compatibility and osteoinductive properties [56, 57].

Despite these promising outcomes, this study is not without limitations. The experimental observation period was relatively short, focusing on early-stage bone repair. However, bone healing is a long-term, dynamic process involving continuous remodeling. Future investigations should extend the follow-up duration to assess long-term degradation kinetics, the impact of degradation by-products on surrounding tissues, and the quality and mechanical integrity of newly formed bone. Additionally, validation in larger animal models (e.g., dogs or sheep) will be essential to approximate clinical conditions and further verify the scaffold's translational potential [47, 48, 58].

In conclusion, the CC/HMS/PLGA composite scaffold, by optimizing the mechanical and biological properties of PLGA, and through regulating acidic degradation by-products, releasing bioactive ions, and constructing a multi-level porous structure, achieved a synergistic enhancement effect at both the cellular and in vivo levels. The results of this study not only confirmed the

significant advantages of the CMP scaffold in promoting bone defect repair, but also provided new ideas for the construction of the next-generation bone repair materials with metabolic coordination and biological functionality.

Conclusion

The ternary composite scaffold constructed in this study exhibited excellent cell compatibility in vitro and promoted the early osteogenic differentiation of MSCs. It also showed lower biotoxicity and significantly enhanced bone regeneration ability in the rabbit femoral condyle defect model. Compared with the control group without $CaCO_3$ doping, the CMP scaffold had more advantages in new bone formation and defect repair. This might be related to the fact that $CaCO_3$ alleviated the acidification of the microenvironment caused by the acidic degradation products of PLGA and released Ca^{2+} signals. Additionally, the porous structure of HMS might provide a favorable cell adhesion environment and stimulate with silicon ions. In conclusion, the CMP scaffold provides a new idea for the development of novel artificial bone materials with good biocompatibility and bone repair potential.

CRediT authorship contribution statement

Honghan Wu: Writing–original draft, Software, Methodology, Investigation.

Junxi Wu: Resources, Methodology, Formal analysis. **Hao Tang:** Validation, Methodology. **Qian Zhong:** Visualization,

Data curation.**Guangquan Zhao:** Visualization, Conceptualization.**Qianyu Xie:** Software, Validation. **Weikang Xu:**review & editing.**Qingde Wa:** Writing - review & editing, Funding acquisition ,Supervision, Conceptualization.

Declaration of competing interest

The authors declare that they have no known competing financial
interests or personal relationships that could have appeared to influence
the work reported in this paper.

Statement of Ethics

All experimental protocols of this study have been approved by the Medical Ethics Committee of Zunyi Medical University, and all methods were carried out in accordance with ARRIVE guidelines and regulations (the anesthesia method used in this study was intramuscular injection of xylazine hydrochloride).

Funding Statement

This study was supported by The National Natural Science Foundation of China (82160577); The Zunyi City Science & Technology Innovation Talent Project (No. [2024] 04).

Data Availability Statement

All data generated or analyzed during this study are include in this published article.

References

[1] Qi J, Zheng Z, Hu L, et al. Development and characterization of cannabidiol-loaded alginate copper hydrogel for repairing open bone defects in vitro[J]. Colloids Surf B Biointerfaces, 2022,212:112339.
[2] Yang J, Zhang L, Ding Q, et al. Flavonoid-Loaded Biomaterials in Bone Defect Repair[J]. Molecules, 2023,28(19).
[3] Liu Y, Xiong W, Li J, et al. Application of dental pulp stem cells for bone regeneration[J]. Front Med (Lausanne), 2024,11:1339573.
[4] Sadek A A, Abd-Elkareem M, Abdelhamid H N, et al. Enhancement of critical-sized bone defect regeneration using UiO-66 nanomaterial in rabbit femurs[J]. BMC Vet Res, 2022,18(1):260.
[5] Liu F, Sun T, An Y, et al. The potential therapeutic role of extracellular vesicles in critical-size bone defects: Spring of cell-free regenerative medicine is coming[J]. Front Bioeng Biotechnol, 2023,11:1050916.
[6] Aldaadaa A, Owji N, Knowles J. Three-dimensional Printing in Maxillofacial Surgery: Hype versus Reality[J]. J Tissue Eng, 2018,9:1544466979.
[7] Wang Z, Yang Y. Application of 3D Printing in Implantable Medical Devices[J]. Biomed Res Int, 2021,2021:6653967.
[8] Zhang Y, Wang T, Li J, et al. Bilayer Membrane Composed of Mineralized Collagen and Chitosan Cast Film Coated With Berberine-Loaded PCL/PVP Electrospun Nanofiber Promotes Bone Regeneration[J]. Front Bioeng Biotechnol, 2021,9:684335.
[9] Xu W, Zhao R, Wu T, et al. Biodegradable calcium carbonate/mesoporous silica/poly(lactic-glycolic acid) microspheres scaffolds with osteogenesis ability for bone regeneration[J]. RSC Adv, 2021,11(9):5055-5064.
[10] Xu W, Wei K, Lin Z, et al. Storage and release of rare earth elements in microsphere-based scaffolds for enhancing osteogenesis[J]. Sci Rep, 2022,12(1):6383.
[11] Song R, Murphy M, Li C, et al. Current development of biodegradable polymeric materials for biomedical applications[J]. Drug Des Devel Ther, 2018,12:3117-3145.
[12] Shiroud Heidari B, Ruan R, Vahabli E, et al. Natural, synthetic and commercially-available biopolymers used to regenerate tendons and ligaments[J]. Bioact Mater, 2023,19:179-197.
[13] Lin Z, Wu J, Qiao W, et al. Precisely controlled delivery of magnesium ions thru sponge-like monodisperse PLGA/nano-MgO-alginate core-shell microsphere device to enable in-situ bone regeneration[J]. Biomaterials, 2018,174:1-16.
[14] Bittner-Frank M, Reisinger A G, Andriotis O G, et al. Cortical and trabecular mechanical properties in the femoral neck vary differently with changes in bone mineral density[J]. JBMR Plus, 2024,8(6):e49.
[15] Smith A N, Ulsh J B, Gupta R, et al. Characterization of degradation kinetics of additively manufactured PLGA under variable mechanical loading paradigms[J]. J Mech Behav Biomed Mater, 2024,153:106457.
[16] Xu D, Xu Z, Cheng L, et al. Improvement of the mechanical properties and

osteogenic activity of 3D-printed polylactic acid porous scaffolds by nano-hydroxyapatite and nano-magnesium oxide[J]. Heliyon, 2022,8(6):e9748.

[17]Owji N, Mandakhbayar N, Cha J, et al. Inclusion of calcium phosphate does not further improve in vitro and in vivo osteogenesis in a novel, highly biocompatible, mechanically stable and 3D printable polymer[J]. Sci Rep, 2022,12(1):16977.

[18]Zhao D, Zhu T, Li J, et al. Poly(lactic-co-glycolic acid)-based composite bone-substitute materials[J]. Bioactive Materials, 2021,6(2):346-360.

[19]Shen M, Wang L, Feng L, et al. bFGF-Loaded Mesoporous Silica Nanoparticles Promote Bone Regeneration Through the Wnt/beta-Catenin Signalling Pathway[J]. Int J Nanomedicine, 2022,17:2593-2608.

[20]Gong S, Lang S, Wang Y, et al. pH-Responsive Mesoporous Silica Nanoparticles Loaded with Naringin for Targeted Osteoclast Inhibition and Bone Regeneration[J]. Int J Nanomedicine, 2024,19:6337-6358.

[21]Liang W, Zhou C, Liu X, et al. Current status of nano-embedded growth factors and stem cells delivery to bone for targeted repair and regeneration[J]. J Orthop Translat, 2025,50:257-273.

[22]Budiman A, Mutmainah L, Anjelina M, et al. The Application of Mesoporous Silica Nanoparticles in Enhancing the Efficacy of Anti-Atherosclerosis Therapies: A Review[J]. Int J Nanomedicine, 2025,20:9825-9856.

[23]Petousis M, Michailidis N, Korlos A, et al. Biomedical Composites of Polycaprolactone/Hydroxyapatite for Bioplotting: Comprehensive Interpretation of the Reinforcement Course[J]. Polymers (Basel), 2024,16(17).

[24]Chen Y, Zhao Q. Innovative modification strategies and emerging applications of natural hydrogel scaffolds for osteoporotic bone defect regeneration[J]. Front Bioeng Biotechnol, 2025,13:1591896.

[25]Shi X, Wang Y, Ren L, et al. Novel mesoporous silica-based antibiotic releasing scaffold for bone repair[J]. Acta Biomater, 2009,5(5):1697-1707.

[26]Liu H, Wen Z, Liu Z, et al. Unlocking the potential of amorphous calcium carbonate: A star ascending in the realm of biomedical application[J]. Acta Pharm Sin B, 2024,14(2):602-622.

[27]Munyemana J C, He H, Fu C, et al. Recombinant Collagen-Templated Biomineralized Synthesis of Biocompatible pH-Responsive Porous Calcium Carbonate Nanospheres[J]. ACS Omega, 2023,8(34):30879-30887.

[28]Xiao S, Wei J, Liu J, et al. In situ comparison of osteogenic effects of polymer-based scaffolds with different degradability by integrated scaffold model[J]. Colloids Surf B Biointerfaces, 2024,241:114047.

[29]Si Y, Dong S, Li M, et al. Curcumin-encapsulated exosomes in bisphosphonate-modified hydrogel microspheres promote bone repair through macrophage polarization and DNA damage mitigation[J]. Mater Today Bio, 2025,32:101874.

[30]Wang G, Lv Z, Wang T, et al. Surface Functionalization of Hydroxyapatite Scaffolds with MgAlEu-LDH Nanosheets for High-Performance Bone Regeneration[J]. Adv Sci (Weinh), 2022,10(1):e2204234.

[31]Shineh G, Janghour L M, Xia Y, et al. Biomolecule-functionalized dental

implant surfaces: Towards augmenting soft tissue integration[J]. Bioact Mater, 2025,53:540-590.

[32]Chen Q, Gu J, Zhang H, et al. Promoting implant osseointegration via the osteoblast-selective beta-amino acid polymer strategy[J]. Nat Commun, 2025,16(1):7190.

[33]Kuten Pella O, Hornyak I, Horvathy D, et al. Albumin as a Biomaterial and Therapeutic Agent in Regenerative Medicine[J]. Int J Mol Sci, 2022,23(18).

[34]Shams F, Jamshidian M, Shaygani H, et al. A study on the cellular adhesion properties of a hybrid scaffold for vascular tissue engineering through molecular dynamics simulation[J]. Sci Rep, 2025,15(1):16433.

[35]Moghaddam A S, Dunne K, Breyer W, et al. Hydrogels with multiple RGD presentations increase cell adhesion and spreading[J]. Acta Biomater, 2025,199:142-153.

[36]Kim J, Jekarl D W, Kim M, et al. Effects of ECM protein mimetics on adhesion and proliferation of chorion derived mesenchymal stem cells[J]. Int J Med Sci, 2014,11(3):298-308.

[37]Xu W, Zhao R, Wu T, et al. Biodegradable calcium carbonate/mesoporous silica/poly(lactic-glycolic acid) microspheres scaffolds with osteogenesis ability for bone regeneration[J]. RSC Adv, 2021,11(9):5055-5064.

[38]Yan B, Hua Y, Wang J, et al. Surface Modification Progress for PLGA-Based Cell Scaffolds[J]. Polymers (Basel), 2024,16(1).

[39]de Carvalho A B G, Rahimnejad M, Oliveira R L M S, et al. Personalized bioceramic grafts for craniomaxillofacial bone regeneration[J]. Int J Oral Sci, 2024,16(1):62.

[40]Zhou J, Xiong S, Liu M, et al. Study on the influence of scaffold morphology and structure on osteogenic performance[J]. Front Bioeng Biotechnol, 2023,11:1127162.

[41]Huang D, Li Z, Li G, et al. Biomimetic structural design in 3D-printed scaffolds for bone tissue engineering[J]. Mater Today Bio, 2025,32:101664.

[42]Aydin M S, Marek N, Luciani T, et al. Impact of Porosity and Stiffness of 3D Printed Polycaprolactone Scaffolds on Osteogenic Differentiation of Human Mesenchymal Stromal Cells and Activation of Dendritic Cells[J]. ACS Biomater Sci Eng, 2024,10(12):7539-7554.

[43]Zebaze R, Atkinson E J, Peng Y, et al. Increased Cortical Porosity and Reduced Trabecular Density Are Not Necessarily Synonymous With Bone Loss and Microstructural Deterioration[J]. JBMR Plus, 2019,3(4):e10078.

[44]Coburn B, Salary R R. Mechanical Characterization of Porous Bone-like Scaffolds with Complex Microstructures for Bone Regeneration[J]. Bioengineering (Basel), 2025,12(4).

[45]Zhang B, Pei Z, He W, et al. 3D-printed porous zinc scaffold combined with bioactive serum exosomes promotes bone defect repair in rabbit radius[J]. Aging (Albany NY), 2024,16(11):9625-9648.

[46]Matsushita A, Kudo T, Tominami K, et al. Frequency-Regulated Repeated Micro-Vibration Promotes Osteoblast Differentiation Through BMP Signaling

in MC3T3-E1 Cells[J]. Life (Basel), 2025,15(4).

[47]Sun Y, Jia X, Meng Q. Characteristic Evaluation of Recombinant MiSp/Poly(lactic-co-glycolic) Acid (PLGA) Nanofiber Scaffolds as Potential Scaffolds for Bone Tissue Engineering[J]. Int J Mol Sci, 2023,24(2).

[48]Contreras-Caceres R, Cabeza L, Perazzoli G, et al. Electrospun Nanofibers: Recent Applications in Drug Delivery and Cancer Therapy[J]. Nanomaterials (Basel), 2019,9(4).

[49]Lian M, Sun B, Qiao Z, et al. Bi-layered electrospun nanofibrous membrane with osteogenic and antibacterial properties for guided bone regeneration[J]. Colloids Surf B Biointerfaces, 2019,176:219-229.

[50]Gentili C, Palama M E F, Sexton G, et al. Sustainably cultured coral scaffold supports human bone marrow mesenchymal stromal cell osteogenesis[J]. Regen Ther, 2024,26:366-381.

[51]Lun D, Li S, Li N, et al. Limitations and modifications in the clinical application of calcium sulfate[J]. Front Surg, 2024,11:1278421.

[52]Viti F, Landini M, Mezzelani A, et al. Osteogenic Differentiation of MSC through Calcium Signaling Activation: Transcriptomics and Functional Analysis[J]. PloS one, 2016,11(2):e148173.

[53]Cheng L, Cai Z, Zhao J, et al. Black phosphorus-based 2D materials for bone therapy[J]. Bioactive materials, 2020,5(4):1026-1043.

[54] Liu T, Li Z, Zhao L, et al. Customized Design 3D Printed PLGA/Calcium Sulfate Scaffold Enhances Mechanical and Biological Properties for Bone Regeneration[J]. Front Bioeng Biotechnol, 2022,10:874931.

[55]Chen X, Wang C, Hao M, et al. Mesoporous Silica Promotes Osteogenesis of Human Adipose-Derived Stem Cells Identified by a High-Throughput Microfluidic Chip Assay[J]. Pharmaceutics, 2022,14(12).

[56]Nii T, Katayama Y. Biomaterial-Assisted Regenerative Medicine[J]. Int J Mol Sci, 2021,22(16).

[57] Min K H, Kim D H, Kim K H, et al. Biomimetic Scaffolds of Calcium-Based Materials for Bone Regeneration[J]. Biomimetics (Basel), 2024,9(9).

[58] Lian M, Sun B, Qiao Z, et al. Bi-layered electrospun nanofibrous membrane with osteogenic and antibacterial properties for guided bone regeneration[J]. Colloids Surf B Biointerfaces, 2019,176:219-229.

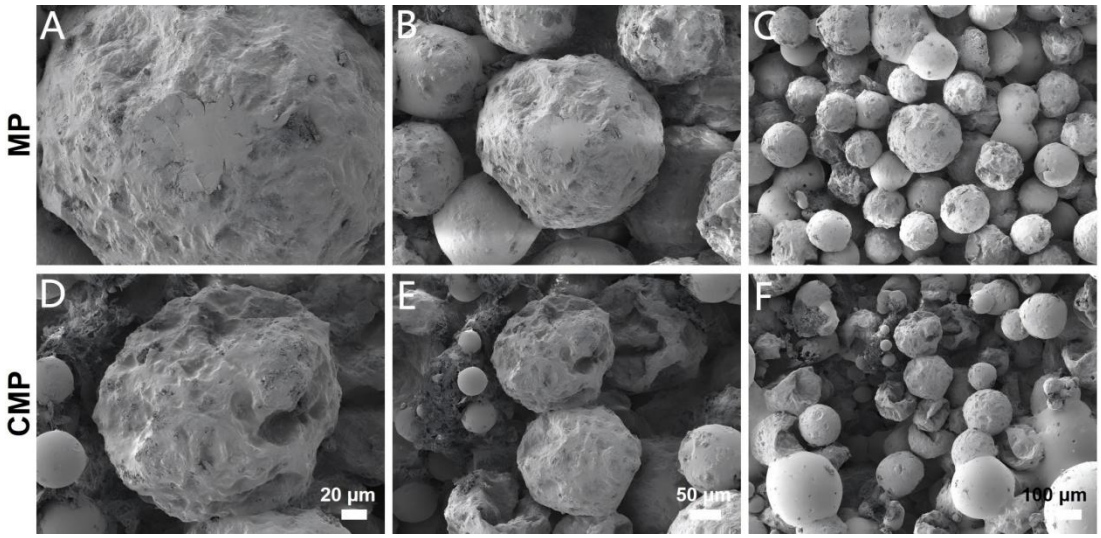

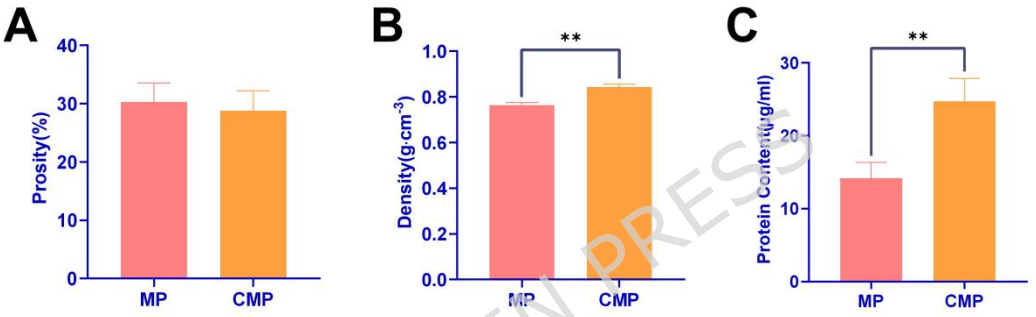

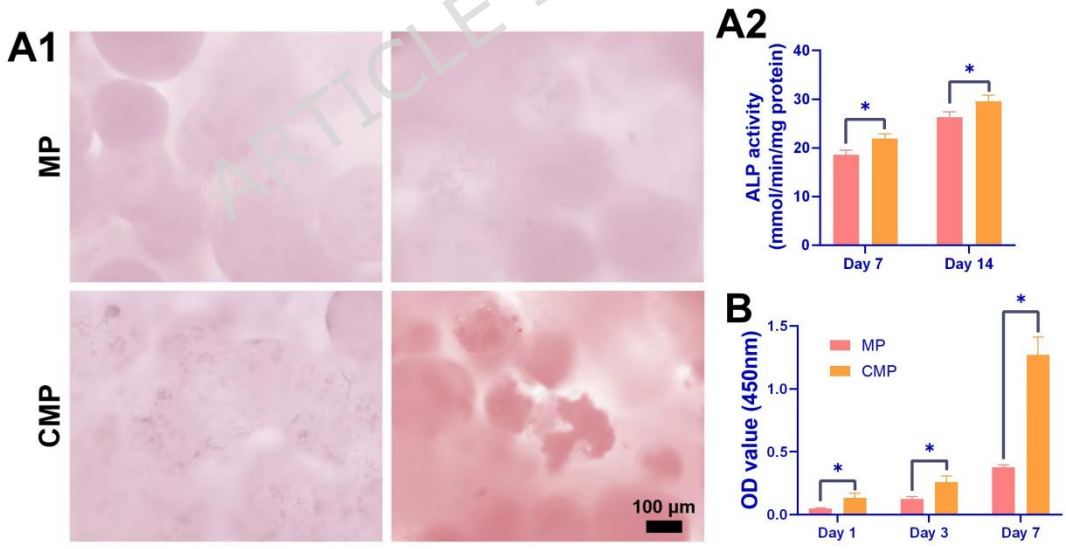

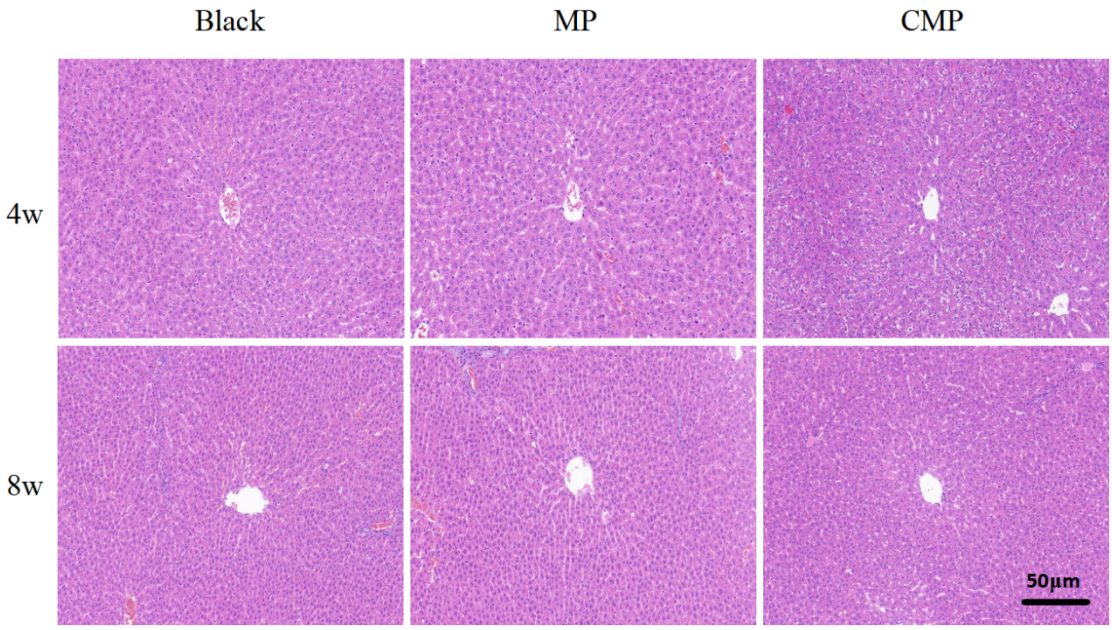

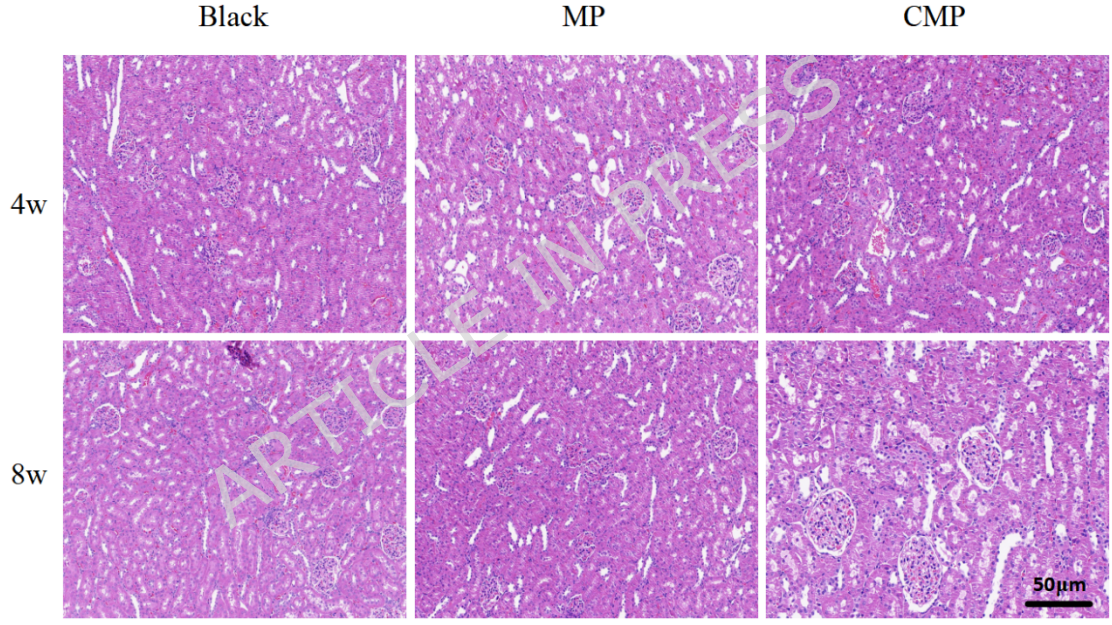

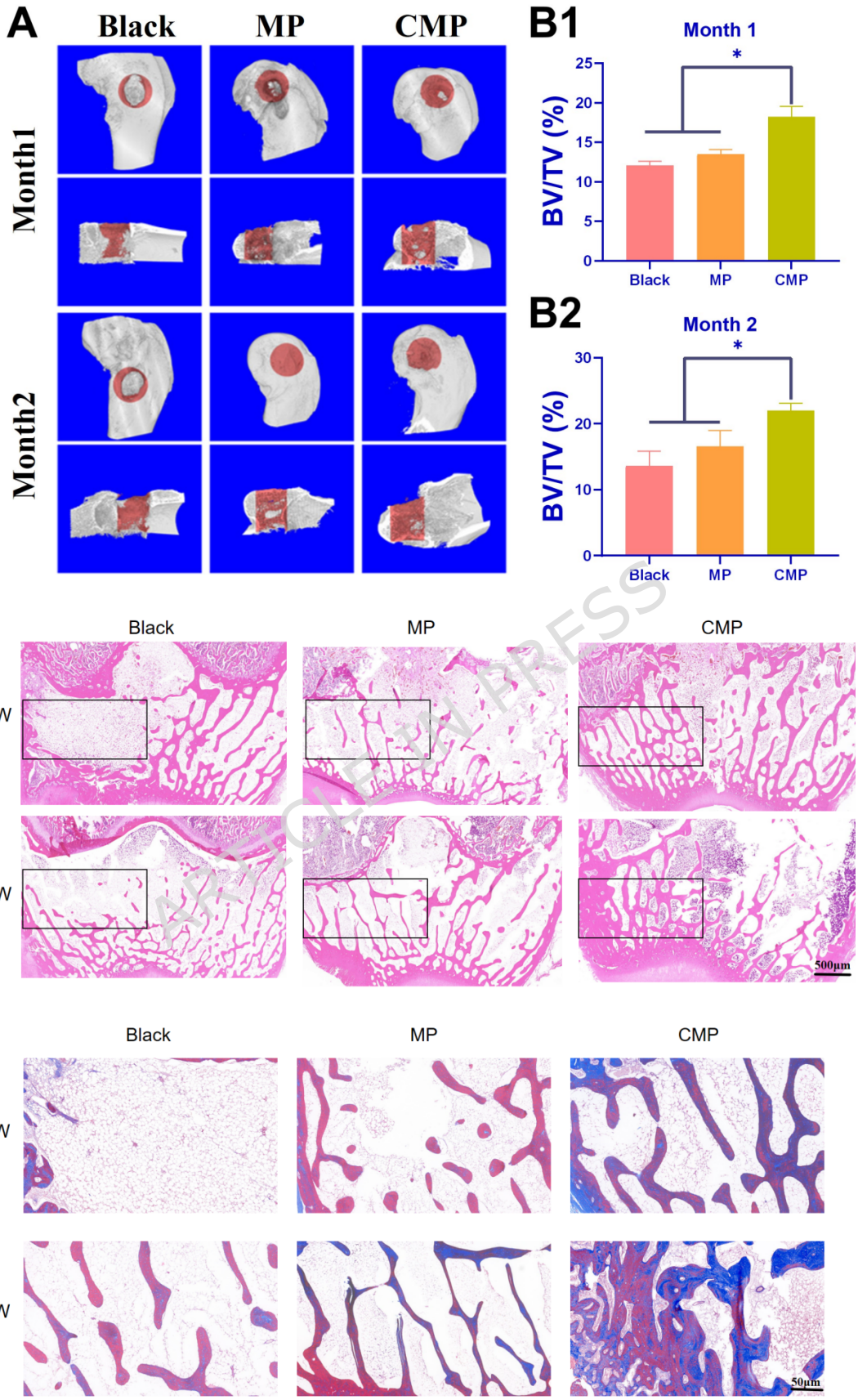

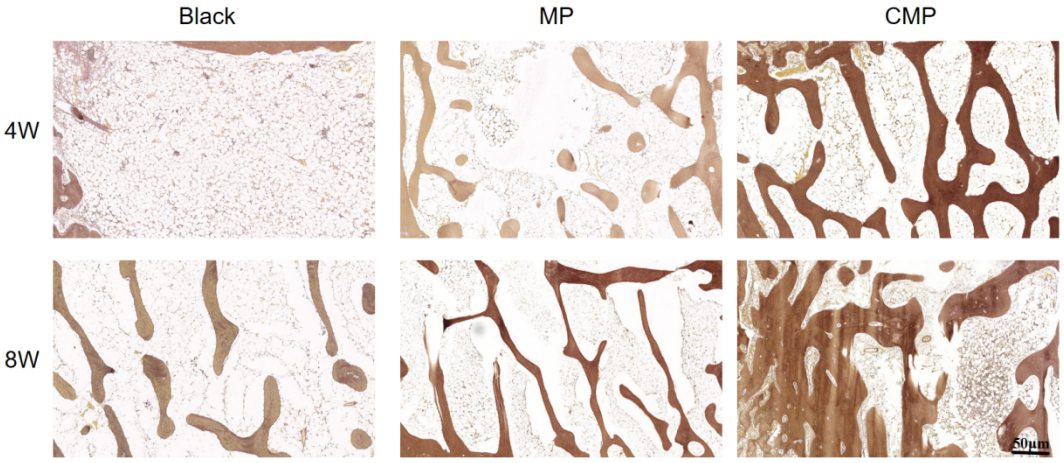

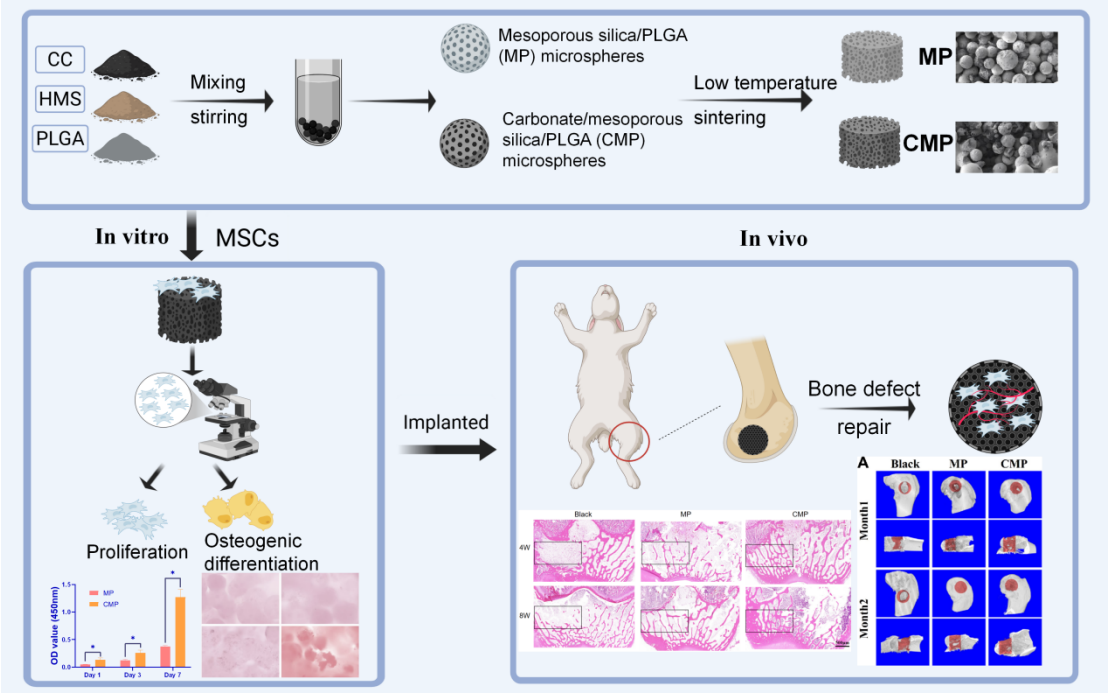

Figure 1 Schematic illustration of the study design.

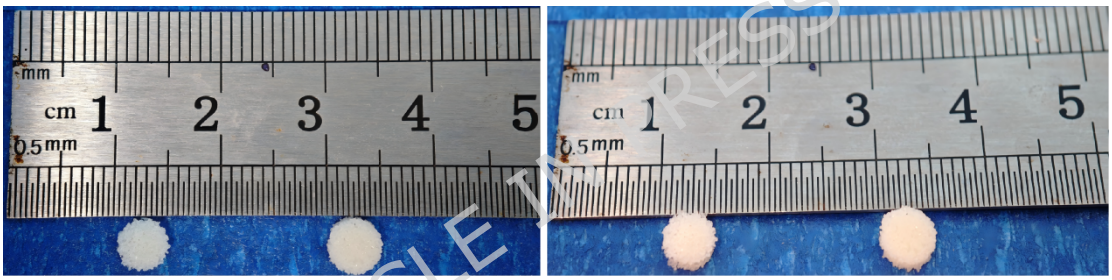

Figure 2 In vivo study of the scaffold(diameter 5mm, height 1mm).

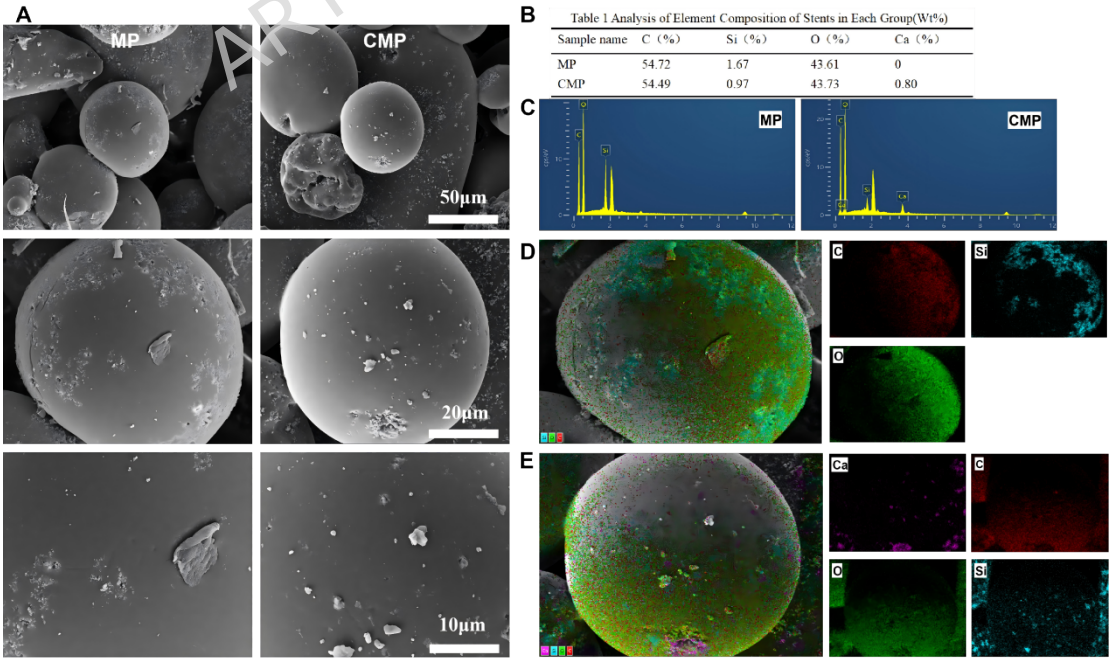

Figure 3. SEM images of MP and CMP scaffolds at different magnifications

(Figure 3A), and EDS analysis of elements on the scaffold surface (Table 1, Figure 3 B-E).

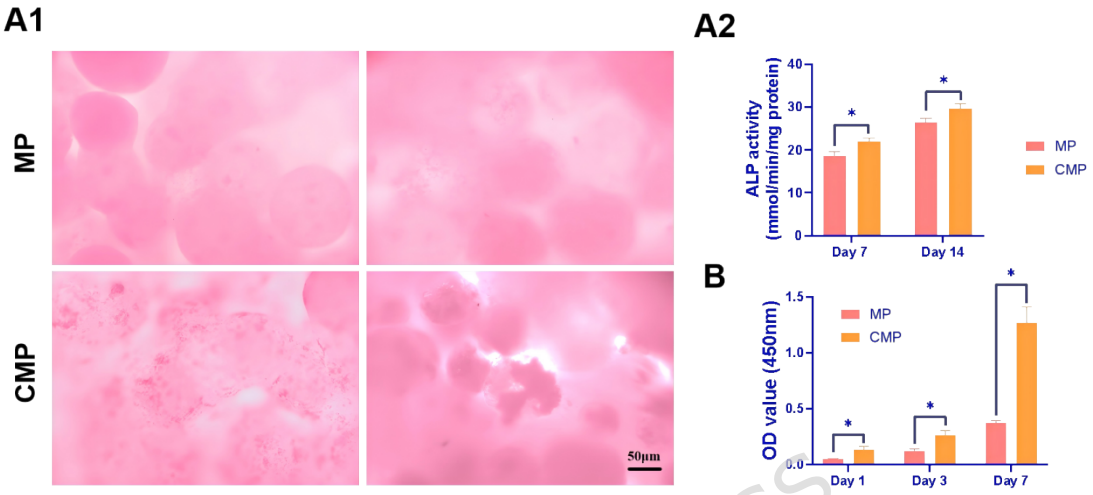

Figure 4. Quantitative analysis of (A) scaffold porosity, (B)scaffold density , and (C) protein adsorption capacity. Data are expressed as mean ± SD. ns: not significant ($P > 0.05$); **: $P < 0.01$.

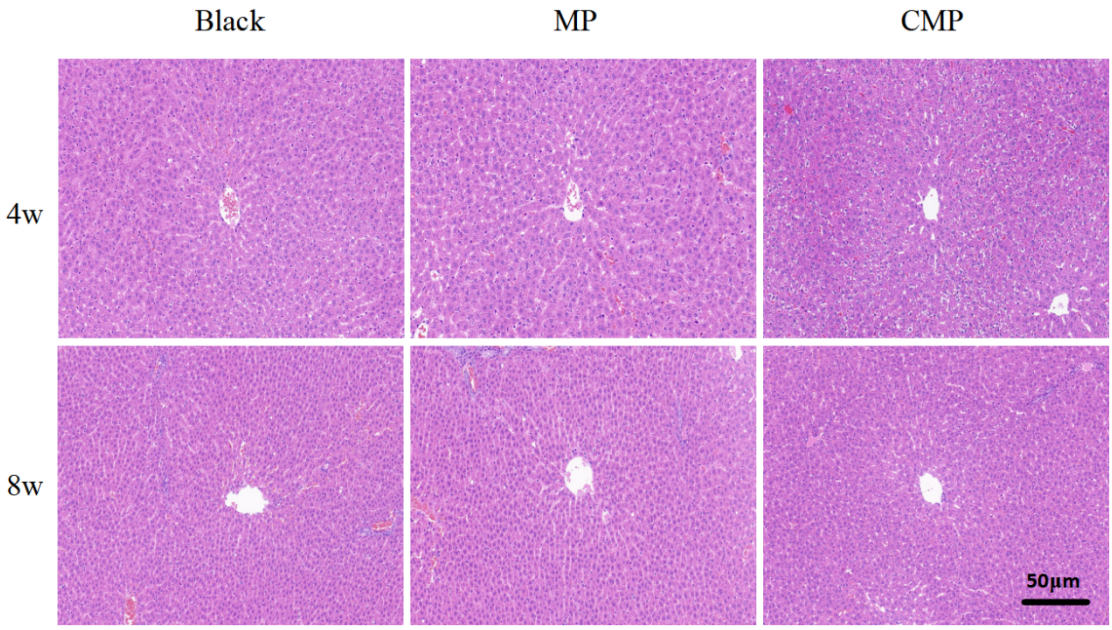

Figure 6. H&E staining of liver tissue at weeks 4 and 8 post-implantation in the blank, MP, and CMP groups (scale bar = 50 μm).

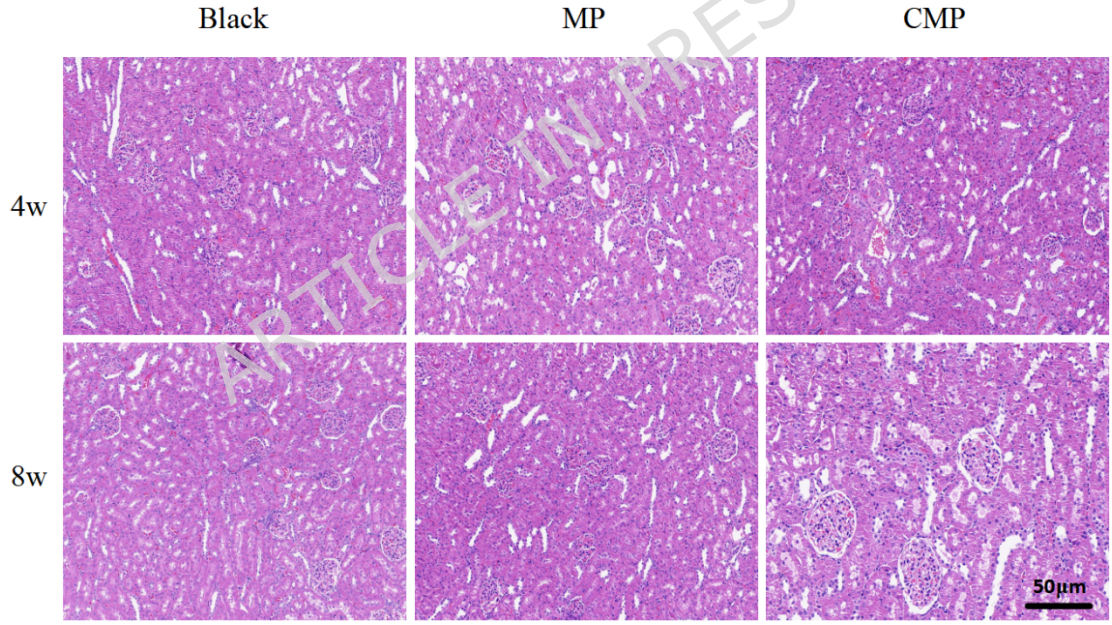

Figure 7. H&E staining of kidney tissue at weeks 4 and 8 post-implantation in the blank, MP, and CMP groups (scale bar = 50 μm).

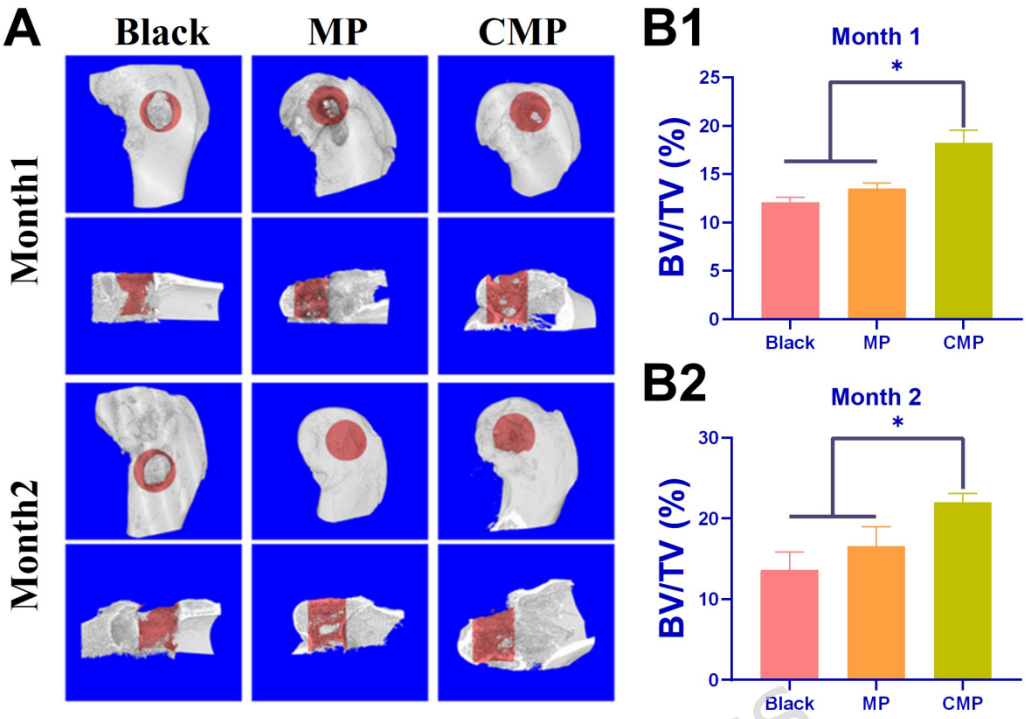

Figure 8. (A) Micro-CT images of the femoral condyle defect sites at 4 and 8 weeks post-surgery. (B) Quantification of bone volume fraction (BV/TV) in the blank, MP, and CMP groups. Data are presented as mean ± SD; *P < 0.05.

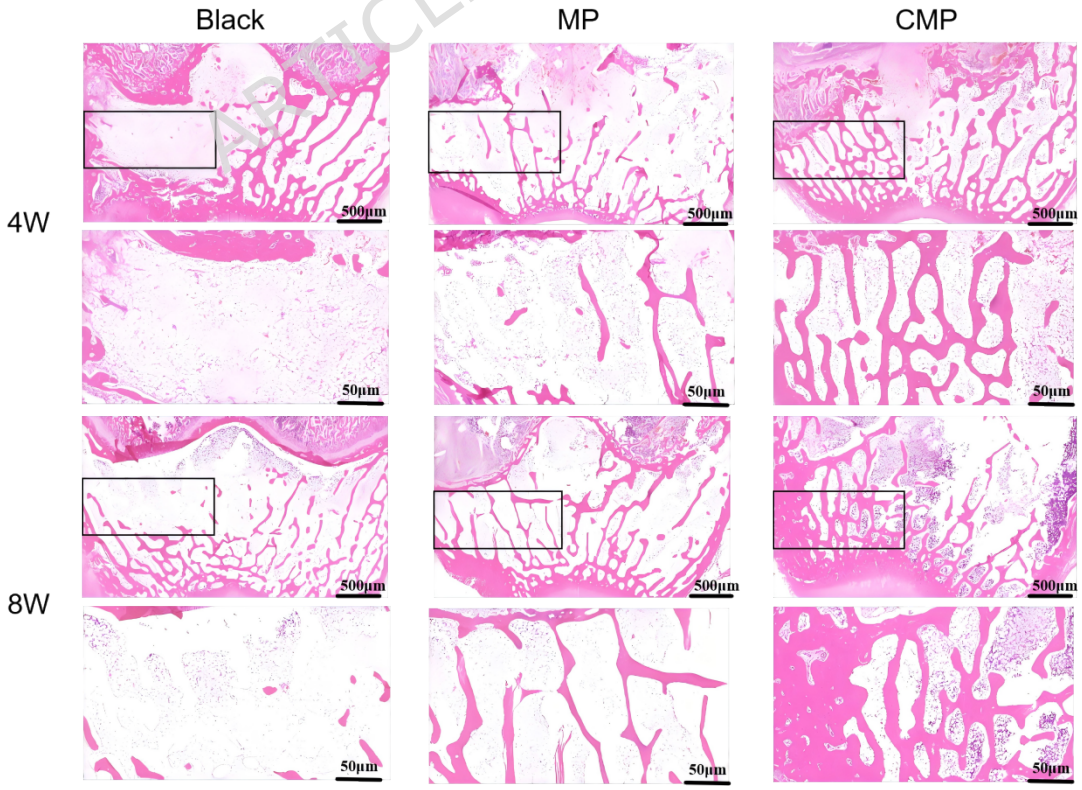

Figure 9. H&E staining of femoral condyle defect regions in the blank, MP,

and CMP groups at 4 and 8 weeks post-surgery.

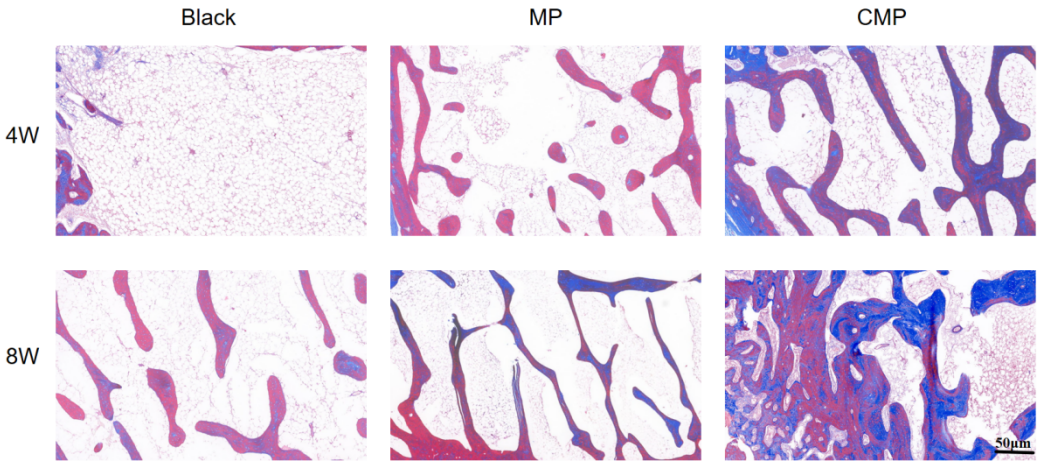

Figure 10. Masson's trichrome staining of bone defect regions in the blank, MP, and CMP groups at 4 and 8 weeks post-surgery (scale bar = 50 μm).

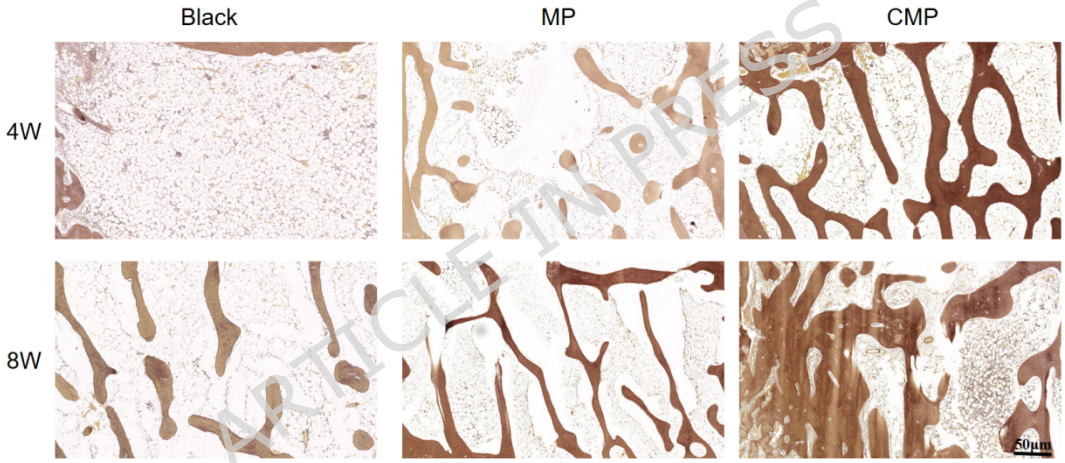

Figure 11. Movat's pentachrome staining of bone defect areas in the blank, MP, and CMP groups at 4 and 8 weeks post-surgery (scale bar = 50 μm).

Table 1. Hematological and liver/kidney function parameters in the blank, MP, and CMP groups at 4 and 8 weeks postoperatively.

	Test index	Black	MP	CMP	*P* value
4 W	WBC(10^9/L)	8.57±0.36	8.36±0.14	8.32±0.17	P=0.45
	RBC(10^{12}/L)	7.56±0.46	7.55±0.36	7.78±0.19	P=0.68
	HB(g/L)	135.33 ± 3.06	138.00±4.58	135.67±4.73	P=0.71
	PLT(10^9/L)	555.33 ± 29.54	565.33 ± 37.21	560.33±39.17	P=0.94
	ALT(U/L)	44.30±3.59	44.37±2.66	47.03±2.73	*P*=0.49
	AST(U/L)	58.13±2.82	58.93±4.24	57.93±3.27	*P*=0.93
	BUN(mmol/L)	14.77±1.96	14.87±1.26	15.10±0.82	*P*=0.96
	Cr(μmol/L)	116.33 ± 4.16	120.67±7.57	120.00±4.36	*P*=0.62
8 W	WBC(10^9/L)	8.54±0.17	8.43±0.59	8.49±0.11	*P*=0.93
	RBC(10^{12}/L)	7.62±0.36	7.43±0.44	7.74±0.28	*P*=0.61
	HB(g/L)	138.00 ± 6.08	136.33±4.73	137.00±3.61	*P*=0.92
	PLT(10^9/L)	565.00 ± 25.87	587.67 ± 12.74	588.33±13.65	*P*=0.29
	ALT(U/L)	47.00±2.89	46.83±3.68	44.20±1.55	*P*=0.45
	AST(U/L)	59.10±2.88	60.37±4.45	59.73±3.29	*P*=0.91
	BUN(mmol/L)	16.07±1.15	15.03±1.63	15.17±1.22	*P*=0.62
	Cr(μmol/L)	117.00 ± 3.00	122.67±5.51	117.67±13.32	*P*=0.69

Table 1 Analysis of Element Composition of Stents in Each Group(Wt%)

Sample name	C（%）	Si（%）	O（%）	Ca（%）
MP	54.72	1.67	43.61	0
CMP	54.49	0.97	43.73	0.80

Table 2. Hematological and liver/kidney function parameters in the blank, MP, and CMP groups at 4 and 8 weeks postoperatively.

	Test index	Black	MP	CMP	*P* value
4 W	WBC(10^9/L)	8.57±0.36	8.36±0.14	8.32±0.17	P=0.45
	RBC(10^{12}/L)	7.56±0.46	7.55±0.36	7.78±0.19	P=0.68
	HB(g/L)	135.33 ± 3.06	138.00±4.58	135.67±4.73	P=0.71
	PLT(10^9/L)	555.33 ± 29.54	565.33 ± 37.21	560.33±39.17	P=0.94
	ALT(U/L)	44.30±3.59	44.37±2.66	47.03±2.73	*P*=0.49
	AST(U/L)	58.13±2.82	58.93±4.24	57.93±3.27	*P*=0.93
	BUN(mmol/L)	14.77±1.96	14.87±1.26	15.10±0.82	*P*=0.96
	Cr(μmol/L)	116.33 ± 4.16	120.67±7.57	120.00±4.36	*P*=0.62
8 W	WBC(10^9/L)	8.54±0.17	8.43±0.59	8.49±0.11	*P*=0.93
	RBC(10^{12}/L)	7.62±0.36	7.43±0.44	7.74±0.28	*P*=0.61
	HB(g/L)	138.00 ± 6.08	136.33±4.73	137.00±3.61	*P*=0.92
	PLT(10^9/L)	565.00 ± 25.87	587.67 ± 12.74	588.33±13.65	*P*=0.29
	ALT(U/L)	47.00±2.89	46.83±3.68	44.20±1.55	*P*=0.45
	AST(U/L)	59.10±2.88	60.37±4.45	59.73±3.29	*P*=0.91
	BUN(mmol/L)	16.07±1.15	15.03±1.63	15.17±1.22	*P*=0.62

Cr(μmol/L)	117.00±3.00	122.67±5.51	117.67±13.32	*P*=0.69